Stony Brook University

Synthesis and Characterization Studies of Li-Fe-In-(PO$_4$) Phases: Chemical Relatives of

Battery Cathode Material Lithium Iron Phosphate

A Thesis Presented

by

Michael R. Saccomanno

to

The Graduate School

in Partial Fulfillment of the

Requirements

for the Degree of

Master of Science

in

Chemistry

Stony Brook University

August 2014

Stony Brook University

The Graduate School

Michael R. Saccomanno

We, the thesis committee for the above candidate for the

Master of Science degree, hereby recommend

acceptance of this thesis.

Peter Khalifah – Thesis Advisor
Assistant Professor, Department of Chemistry

Amy C. Marschilok – Chair
Research Associate Professor, Department of Chemistry

John B. Parise – Third Member
Distinguished Professor, Departments of Chemistry and Geosciences

This thesis is accepted by the Graduate School

Charles Taber
Dean of the Graduate School

Abstract of the Thesis

Synthesis and Characterization Studies of Li-Fe-In-(PO$_4$) Phases: Chemical Relatives of

Battery Cathode Material Lithium Iron Phosphate

by

Michael R. Saccomanno

Master of Science

in

Chemistry

Stony Brook University

2014

Lithium iron(II) phosphate, also known as lithium ferrophosphate (LiFePO$_4$, LFP), has been the subject of many recent energy storage studies. As a battery cathode material, LFP has many advantages for commercial applications. Compared to its competitors like LiMn$_2$O$_4$ and the ubiquitous but carcinogenic LiCoO$_2$, LFP (specific energy = 600 Wh·kg^{-1}) exhibits low toxicity, low cost, good thermal stability, and excellent electrochemical performance at high charge/discharge rates. As part of the efforts to understand and improve LFP, a great amount of research has been committed towards developing, characterizing, and electrochemically testing chemical relatives of this phase. In this work, chemical relatives of LFP belonging to the Li$_3$PO$_4$-Fe$_3$(PO$_4$)$_2$-InPO$_4$ phase system were investigated. This has lead to the discovery of lithium iron(II) indium phosphate [LiFeIn(PO$_4$)$_2$, LFIP]. Structural studies on LFIP using laboratory and synchrotron X-ray, neutron, and electron diffraction techniques have demonstrated this phase to

crystallize in the orthorhombic space group *Pbca* with lattice parameters $a = 9.276(1)$ Å, $b = 13.757(2)$ Å, and $c = 9.476(1)$ Å. Unlike LFP, this new material does not perform well as a battery cathode as found by chemical delithiation tests, electrochemical cycling, and bond-valence sum difference maps of Li^+ diffusion pathways. LFIP has also been characterized by magnetic and optical measurements. The material does not order magnetically above 2 K, is paramagnetic with weak antiferromagnetic interactions, and has an effective magnetic moment of 5.39 μ_B/Fe. LFIP has a band-gap energy of 2.94 eV and d orbital ligand field splitting energies of 0.75 eV and 0.99 eV. Based on our synthesis results, a preliminary assessment of the Li_3PO_4-$Fe_3(PO_4)_2$-$InPO_4$ phase system is presented.

Dedication

The work of this thesis is wholeheartedly dedicated to the members of Stony Brook University's Catholic Campus Ministry, whose inspiring witness to Christ in their daily lives has been an immeasurable source of faith, hope, and love in my formation as a child of God.

"Iron is sharpened by iron; one person sharpens another."

- Proverbs 27:17

Table of Contents

List of Figures

List of Tables

List of Abbreviations

1D – One-Dimensional

2D – Two-Dimensional

BVS – Bond-Valence Sum (Map)

DFT – Density-Functional Theory

EDP – Electron Diffraction Pattern

EDX – Energy-Dispersive X-Ray (Spectroscopy)

GGA – Generalized-Gradient Approximation

GITT – Galvanostatic Intermittent Titration Technique

H5N – 95% Nitrogen / 5% Hydrogen Gas Blend (HydroStar$^®$)

HAADF-STEM – High-Angle Annular Dark-Field Scanning Transmission Electron Microscopy

LCIP – Lithium Cobalt(II) Indium Phosphate, composition unknown [$Li_wCo_xIn_y(PO_4)_z$]

LFP – Lithium Iron(II) Phosphate, $LiFePO_4$ (also "lithium ferrophosphate")

LFIP – Lithium Iron(II) Indium Phosphate, $LiFeIn(PO_4)_2$ [equivalent to $Li_{1.5}Fe_{1.5}In_{1.5}(PO_4)_3$]

MATPASS – Magic-Angle Turning and Phase-Adjusted Sideband Separation

MW-ST – Microwave-Assisted Solvothermal

NASICON – Sodium Super Ion Conductor(s)

NIR-Vis – Near-Infrared-Visible Reflectance (Spectroscopy)

NMR – Nuclear Magnetic Resonance (Spectroscopy)

OCV – Open-Circuit Voltage

PXRD – Powder X-Ray Diffraction

SEM – Scanning Electron Microscopy

UV-Vis – Ultraviolet-Visible (Diffuse Reflectance Spectroscopy)

XRD – X-Ray Diffraction

Acknowledgments

First and foremost, I thank God Almighty for being my solace and my strength throughout life and for instilling in me the curiosity to explore and understand the wonders of His vast Creation.

I would like to thank Prof. Peter Khalifah for granting me the opportunity to conduct research as part of his lab group while I was an undergraduate and for agreeing to be my thesis advisor for my graduate work. His expertise in crystallography and inorganic chemistry has been impressive and edifying during my tenure. I would also like to thank Prof. Clare P. Grey for her insights concerning further studies of the materials discussed herein.

I offer my gratitude to Dr. Yuri Janssen, who was instrumental in initiating me into and regularly supporting me throughout the projects which constitute this work, and to Jue Liu (SEM, EDX), Huafeng Huang (UV-Vis, NIR-Vis), Natalya Chernova at SUNY Binghamton (magnetic measurements), and Lijun Wu at Brookhaven National Laboratory's Condensed Matter Physics and Materials Science Department (EDP) for conducting collaborative experimental work on these materials. I give my thanks to Mr. Liu and Dr. Shou-Hang Bo, formerly of the Grey Group, for being instructors and allies over the course of my research endeavors. I would like to also acknowledge the other Khalifah Group members for providing a hospitable work environment and for their occasional advice.

I would like to thank Prof. Amy C. Marschilok (Chair) and Prof. John B. Parise (Third Member) for their service on my thesis committee and their aid during my M.S. defense.

Lastly, I would like to express my warmest and deepest appreciation to the family members and friends who have bolstered me in every human regard during this challenging process. To their kindness and encouragement I am greatly indebted.

I. INTRODUCTION

Overview

Lithium iron(II) phosphate, or lithium ferrophosphate (LFP), has been the subject of many recent studies concerning the future of energy storage technologies. Ushered in by the pervasive transition to high-capacity Li-ion batteries in computer, communication, and consumer electronics products,[1] LFP as a battery cathode material has been shown to exhibit many desirable qualities, including low toxicity, low cost, good thermal stability, and excellent electrochemical performance at high charge/discharge rates with a specific energy of 600 Wh · kg^{-1}.[2,3,4] These characteristics also make LFP a strong candidate for implementation in the electric vehicle industry, ahead of its lower-performing, more dangerous, and more expensive commercial competitors, including lithium manganese(III,IV) oxide ($LiMn_2O_4$) and the ubiquitous but carcinogenic lithium cobalt(III) oxide ($LiCoO_2$).[1]

Figure 1: The Buckeye Bullet Electric Streamliner used A123 Systems' $LiFePO_4$ batteries to set a land speed world record of 307.66 mph. Photo credit: http://www.a123systems.com/lithium-iron-phosphate-battery.htm.
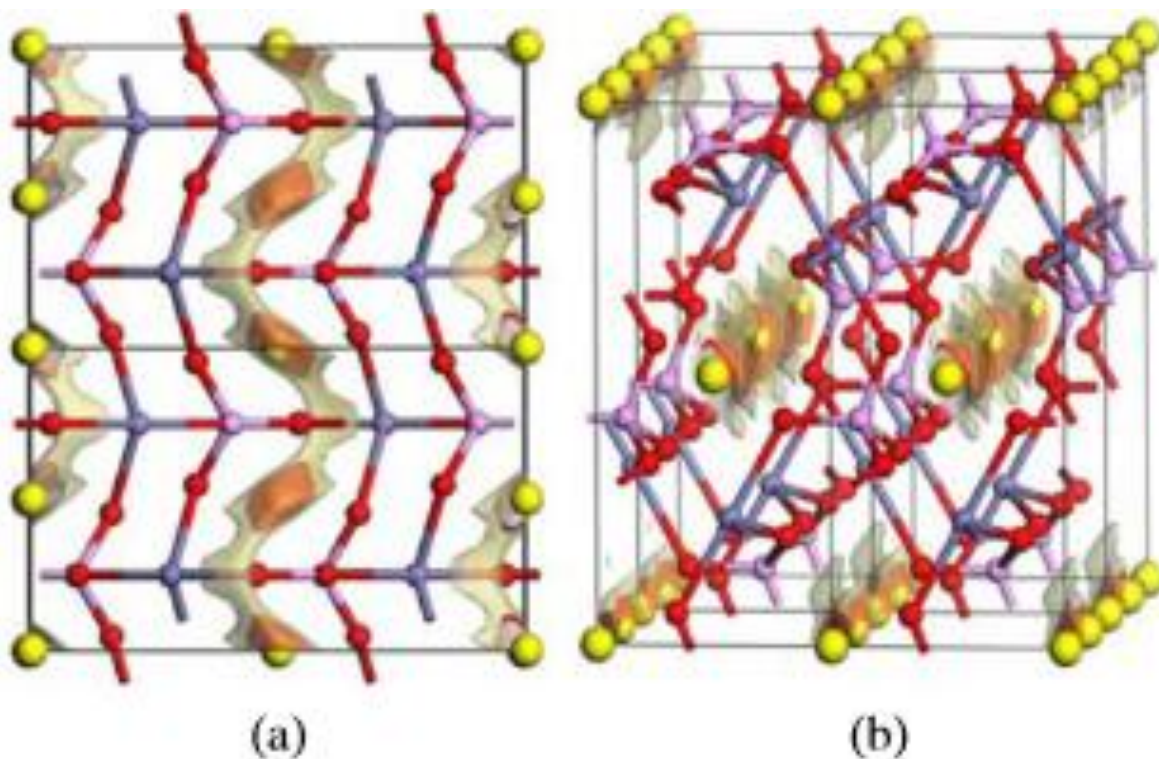
Figure 2: Bond-valence pathway model of one-dimensional (1D) Li^+ diffusion pathways in the fully ordered $LiFePO_4$ structure, projected on (a) the *a-b* plane and (b) the approximate *a-c* plane. Reproduced with permission from Adams, S. *J. Solid State Electrochem.* **2010**, *14*(10), 1787. Copyright 2010.

The robust electrochemical properties of LFP can be very much attributed to its crystal structure. The Li ions in its olivine-like structure [*Pnma*, a = 10.3296 Å, b = 6.0116 Å, c = 4.7018 Å, V = 292.0 Å^3][5] are arranged in 1D edge-sharing chains of LiO_6 octahedra oriented along the *b*-axis.[2] Consistent with phenomenological bond-valence sum maps[6] and quantitative density functional theory[7,8] (DFT) calculations, neutron diffraction experiments analyzed by maximum entropy methods[9] have shown that Li-ion mobility is highly anisotropic along this zigzagging pathway during both intercalation and deintercalation (Figure 2). Accordingly, understanding the structural behavior of the material as a function of its Li content has become one focus of our research efforts. In particular, we hope to better characterize the structural changes that occur between LFP and its delithiated counterpart, $FePO_4$ [*Pnma*, a = 9.85 Å, b = 5.77 Å, c = 4.79 Å, V = 272.2 Å^3][10] and its other chemical relatives.

Basics of Li-Ion Battery Electrochemistry

Components and Operation of an Electrochemical Storage Unit (Battery)

A typical battery contains two oppositely charged electrodes – an anode and a cathode – separated by an electrolytic medium that allows for ion transport between them.[11] During the discharge of a battery, the anode functions as the ion donor and the cathode as the ion acceptor. Commercially viable batteries must contain electrodes that are good ionic and electronic conductors in order to prevent resistive losses. Oftentimes, the electronic conductivity of an electrode active material can be improved by the addition of carbon black, since the former frequently is not a good electronic conductor.

Batteries are classified as being either primary or secondary. Primary batteries are single-use units because the materials are irreversibly changed following discharge, whereas secondary batteries – the focus of extensive research – are capable of being discharged and recharged reversibly for many cycles. Refer to Figure 3 for an illustration of the construction and function of a secondary battery. While secondary batteries usually have lower energy densities per cycle than primary batteries, the cyclability of the former grants them a distinct advantage in terms of lifetime energy output.

Ionic and Electronic Conductivity during the Cycling Process

Li-ion batteries hold such prominent commercial potential largely because of the high energy output afforded by the electro- and physicochemical properties of Li.[12] Being the lightest metal, Li^+ is a prime candidate for transfer between the cathode and anode of a secondary battery. During battery discharge the anode is electrochemically oxidized, resulting in the deintercalation (release) of Li^+ into the electrolyte as electrons travel through an external circuit

3

towards the cathode. To compensate for the negative charge flow in the external circuit, Li^+ intercalates (inserts) into the cathode. During charging, the reverse processes occur. Refer to Figure 3 for an illustration of these processes.
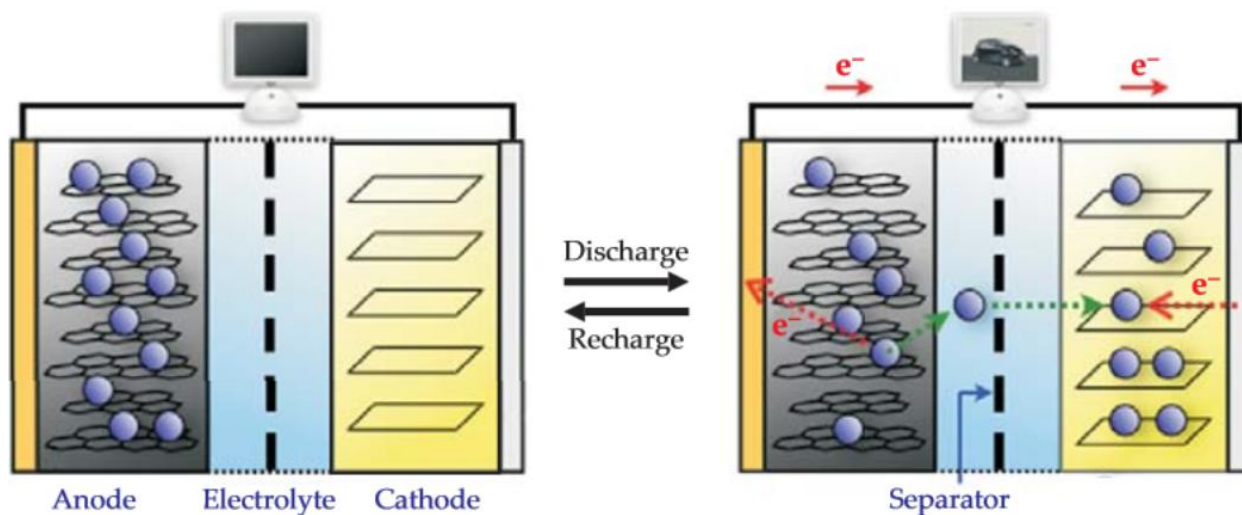
Figure 3: Charging/discharging processes in a secondary Li-ion battery. Reproduced with permission from Abruña, H. D.; Kiya, Y.; Henderson, J. C. *Physics Today* **2008**, *61*(12), 43. Copyright 2008, American Institute of Physics.

Theoretical vs. Actual Capacity and C-Rate

The theoretical capacity of a material is the hypothetical maximum electrical charge the material can hold and hence determines the amount of power a battery constructed from that material can deliver on a single charge. Theoretical capacity in $mAh \cdot g^{-1}$ can be calculated using Equation 1:

$$(1) \text{ Theoretical capacity} = \frac{nF}{3600 * M} \text{ mAh·g}^{-1}$$

where *n* is the number of moles of charge carriers per mole of material, *F* is the Faraday constant $(96,485.3365 \text{ C·mol}^{-1})$, and *M* is the molar mass of the material in units of $kg \cdot mol^{-1}$.

Actual capacity is typically less than the theoretical value due to kinetic restrictions, which inhibit the requisite flow of ions through the material. Impurities and/or heterogeneities may play a minor role as well. The capacity of the material generally decreases with an

increasing number of cycles because of changes in the electrochemical equilibrium between and structural deformations in the cathode and anode upon cycling.

The C-rate corresponds to the rate relative to a material's capacity at which a constant current is held during a single charge or discharge. For example, the notation of C/20 is understood to mean 20 hours per charge or discharge, whereas 2C represents one half-hour per charge or discharge. As a battery's capacity diminishes with use, a given C-rate causes the material to discharge (or charge) in increasingly shorter amounts of time, *i.e.* leading to a shorter usable lifetime per cycle.

Lithium Iron Phosphate Cathode Synthesis and Characterization

Research into the use of LFP as a battery cathode (theoretical capacity = 169.9 mAh·g^{-1}) was largely sparked by the work of Padhi, *et al.*[13] Their work on the reversible chemical delithiation/lithiation of LFP and its electrochemical performance demonstrated that the material was capable of achieving specific capacities in excess of 120 mAh·g^{-1}. In fact, the specific capacities appeared to increase with the cycle number in both the delithiated LFP (Figure 4) and the lithiated FePO$_4$ (Figure 5) samples. The cathode charging half-reaction/Li extraction in this system can be represented by:

$$(2) \ \mathrm{LiFePO_4} - x \ \mathrm{Li^+} - x \ \mathrm{e^-} \rightarrow x \ \mathrm{FePO_4} + (1-x) \ \mathrm{LiFePO_4}$$
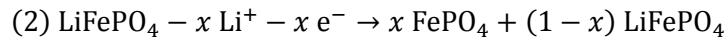
while the cathode discharging half-reaction/Li insertion can be written as:

$$(3) \ \mathrm{FePO_4} + x \ \mathrm{Li^+} + x \ \mathrm{e^-} \rightarrow x \ \mathrm{LiFePO_4} + (1-x) \ \mathrm{FePO_4}$$
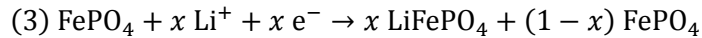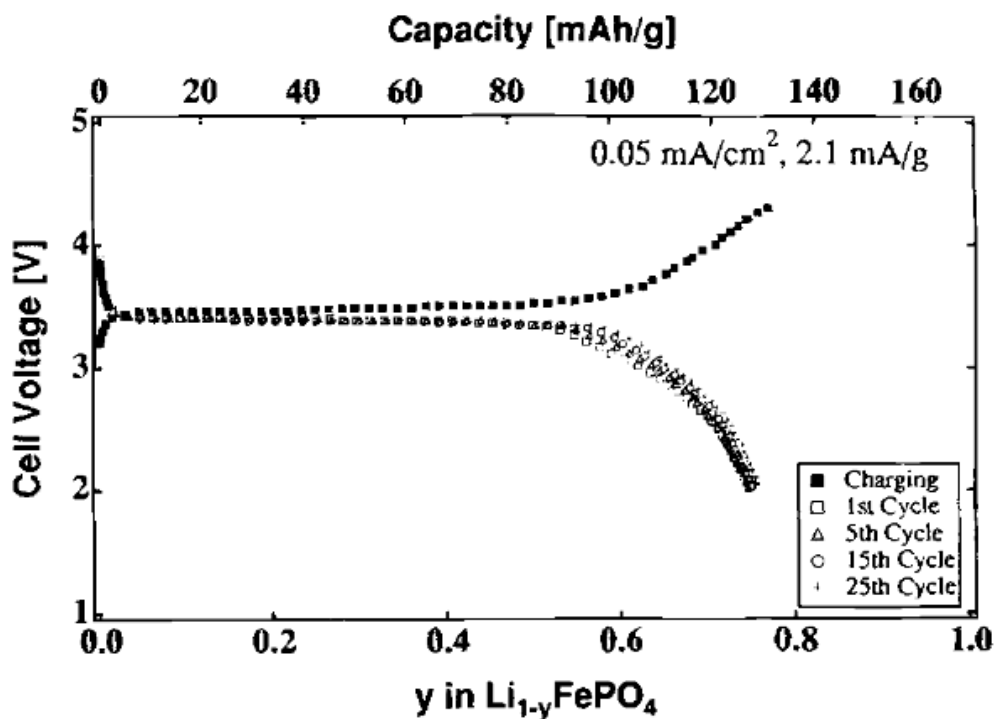
Figure 4: Discharge/charge curves *vs.* Li for delithiated LFP at current density 2.1 mA/g (0.05 mA/cm^2). Reproduced with permission from Padhi, A. K.; Nanjundaswamy, K. S.; Goodenough, J. B. *J. Electrochem. Soc.* **1997**, *144*(4), 1188. Copyright 1997 The Electrochemical Society.
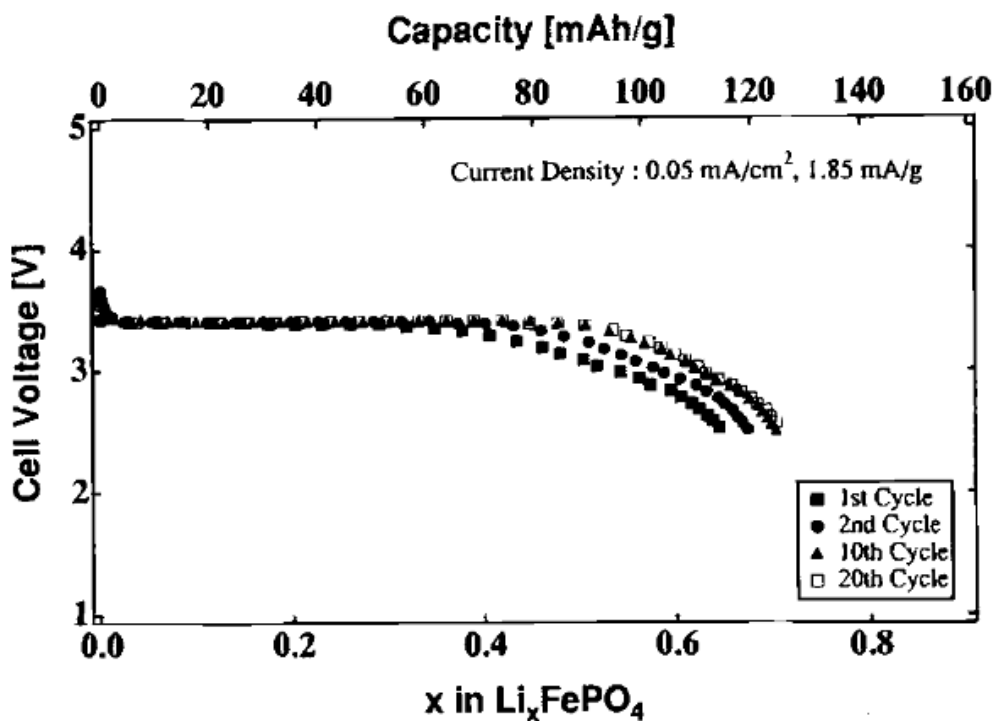
Figure 5: Discharge/charge curves *vs.* Li for lithiated FePO$_4$ at current density 1.85 mA/g (0.05 mA/cm^2). Reproduced with permission from Padhi, A. K.; Nanjundaswamy, K. S.; Goodenough, J. B. *J. Electrochem. Soc.* **1997**, *144*(4), 1188. Copyright 1997 The Electrochemical Society.

Moreover, Padhi, *et al.*[14] sought to understand how the structure of an iron phosphate affects the Fe^{3+}/Fe^{2+} redox couple. They prepared $Li_3Fe_2(PO_4)_3$, $LiFeP_2O_7$, $Fe_4(P_2O_7)_3$, and LFP, and studied their electrochemical performance through cycling measurements. The differences in the P-O bond lengths and the Fe linkages led to significant dissimilarities in the Fe^{3+}/Fe^{2+} redox couples, affirming the importance of structure in the iron phosphate cathode half-reactions, even when the same polyanions are used (Figure 6). Indeed, the redox potential of LFP (3.5 eV) well exceeded those of the other phosphates tested.
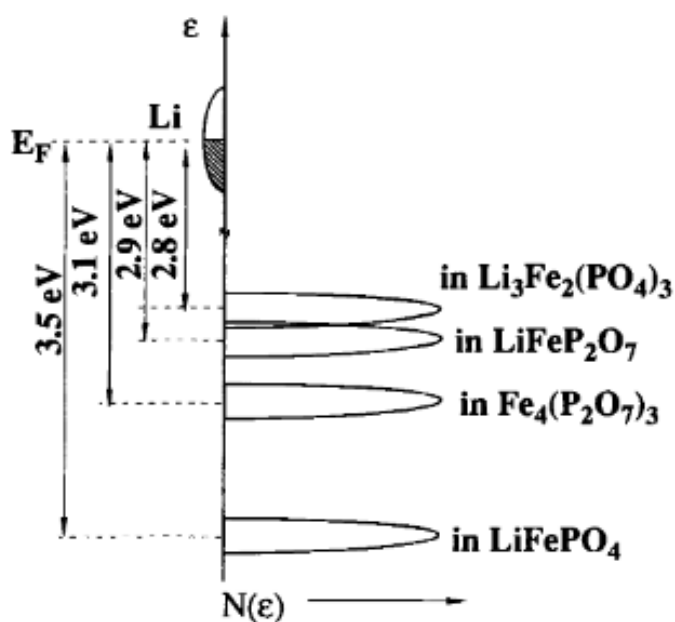
Figure 6: Energy levels of the Fe^{3+}/Fe^{2+} redox couples in different iron phosphates relative to Li. The redox potential in LFP at 3.5 eV below the Fermi level of Li well exceeds those of the others studied. Reproduced with permission from Padhi, A. K.; Nanjundaswamy, K. S.; Masquelier, C.; Okada, S.; Goodenough, J. B. *J. Electrochem. Soc.* **1997**, *144*(5), 1609. Copyright 1997 The Electrochemical Society.

Numerous papers have since been published with the intent of elucidating the structure of LFP and characterizing its electronic and ionic transport properties.[15,16] Hoang and Johannes[3] used first-principles DFT calculations to study native point defects and defect complexes which they characterized by their formation energies as determined within the GGA+U framework, an expansion on the generalized-gradient approximation (GGA) devised by Perdew, *et al.*[17] This revised method takes into account the Hubbard parameter U which was used to relate the single

particle potentials to the magnetic- and orbital-order parameters for the Fe^{2+} cation following the model-Hamiltonian approach.[18,19] Wang, *et al.*[20] also used the GGA+*U* framework to study the surface properties of LFP. Chung, *et al.*[21] directly observed the Fe_{Li} defects in LFP – wherein iron occupies the lithium sites – using aberration-corrected high-angle annular dark-field scanning transmission electron microscopy (HAADF-STEM). These defects seemed to increase in likelihood with increasing annealing temperature (Figure 7).
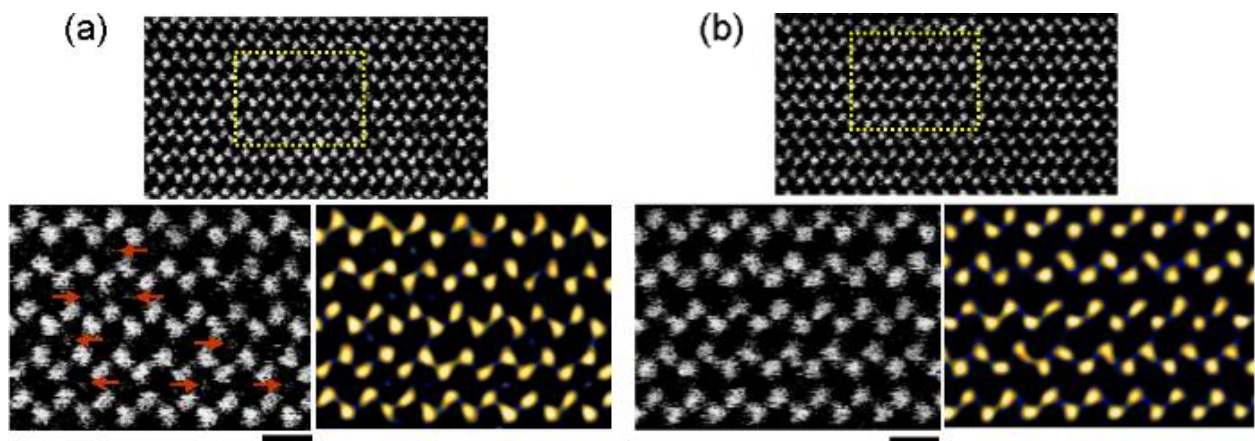
Figure 7: HAADF-STEM images and magnified regions thereof for $LiFePO_4$ crystals with a [010] zone. (a) After annealing at 600 °C, some Li columns have a significantly bright and intense contrast (indicated by red arrows) while still ordered along the Fe-P contours. (b) After annealing at 800 °C, no visible intensities are observed. The deconvoluted images have also been recolored at right of each respective magnified image. Scale bars are 5 Å. Reproduced with permission from Chung, S.-Y.; Choi, S.-Y.; Yamamoto, T.; Ikuhara, Y. *Phys. Rev. Lett.* **2008**, *100*(12), 125502. Copyright 2008 The American Physical Society.

Liang, *et al.*[22] reported on the theoretical and experimental anisotropies in the magnetic properties and X-ray absorption spectra of single-crystal LFP. They developed a mean-field theory to model the significant anisotropies in the Lande *g*-factor, effective moment, and paramagnetic Curie temperature of the LFP crystals, the second of which was found to be consistent with calculations from neutron diffraction data (Table 1).

Table 1: T_N Values and the Result of Fitting Magnetic Susceptibility Curves to a Modified Curie-Weiss Law for Single-Crystal LiFePO$_4$. Reproduced with permission from Liang, G.; Park, K.; Li, J.; Benson, R. E.; Vaknin, D.; Markert, J. T.; Croft, M. C. *Phys. Rev. B: Condens. Matter* **2008**, *77*(6), 64414. Copyright 2008 The American Physical Society.

Axis	T_N (K)	C (emu K/mol)	θ (K)	g	Λ (cm)	μ_{eff} (μ_B)
b (‖)	51	3.685	-59.7 ± 1.7	2.22	0.00138	5.43 ± 0.02
a (⊥,a)	51	3.412	-80.9 ± 1.3	2.13	0.00085	5.22 ± 0.02
c (⊥,c)	51	3.058	-105.7 ± 1.5	2.02	0.00012	4.95 ± 0.02
Average	51	3.385	-82.1 ± 1.5	2.12	0.00076	5.20 ± 0.02

Li, *et al.*[23] examined the Li$^+$ ion conductivity in single-crystal LFP and determined that despite the quasi-2D crystal structure the diffusion is by and large restricted to 1D transport along the *b*-axis in the *Pnma* space group, refuting earlier work by Amin, *et al.*[24] who described the ionic conductivity as virtually two-dimensional (2D) in the *b-c* plane. Weichert, *et al.*[25] also examined the transport properties of LFP using SEM. They found that chemical delithiation of single-crystal LFP formed a cracked, porous FePO$_4$ layer arising from the considerably different molar volumes of the compounds (Figure 8). This porosity and crack formation enhanced bulk transport in the material, which is an advantage for designing cathodes from coarse-grained LFP powders. Such phase boundaries were also observed by Chen, *et al.*[26]
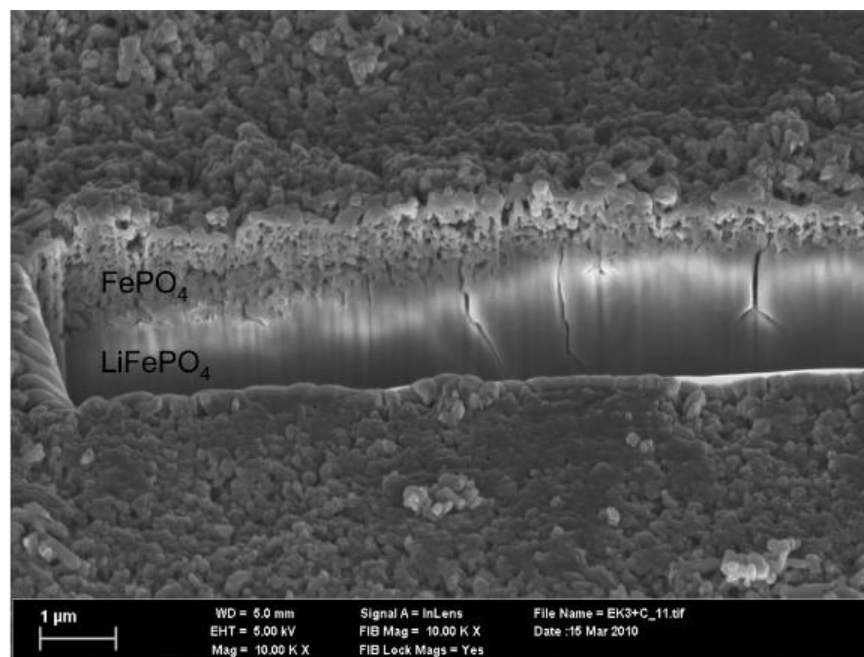
Figure 8: SEM image of a partially delithiated $LiFePO_4$ single crystal. The $FePO_4$ layer exhibits significant crack formation and high porosity. Magnification is 10,000 X. Reproduced with permission from Weichert, K.; Sigle, W.; van Aken, P. A.; Jamnik, J.; Zhu, C.; Amin, R.; Acartürk, T.; Starke, U.; Maier, J. *J. Am. Chem. Soc.* **2012**, *134*(6), 2988. Copyright 2012 American Chemical Society.

Many synthetic techniques to produce electron- and ion-conductive LFP in addition to solid-state reaction have been attempted, including sol-gel,[27] microwave,[28] and floating-zone growth[29] processes. In particular, hydrothermal[30] synthesis of LFP holds promise as a cost-effective and energy-efficient manufacturing process, avoiding the cation disorder thermally induced in samples made at higher synthesis temperatures.[31] However, such a method often yields products with antisite defects, dampening lithium-ion mobility. Chen and Graetz[32] demonstrated using time-resolved *in situ* synchrotron XRD data that these defects could be eliminated above 500 °C. This suggests that a relatively mild heat treatment after hydrothermal synthesis would greatly improve the material's electrochemical performance. This was confirmed by electrochemical cycling measurements, with a notable increase in the specific capacity observed from as-synthesized LFP (80 mAh·g^{-1}) to heat-treated LFP (130 mAh·g^{-1}; 10 minutes at 500 °C) at a rate of C/20.
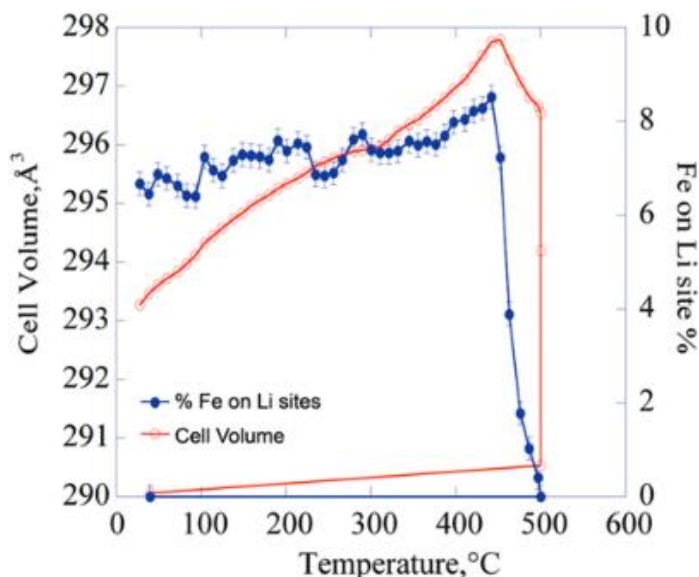
Figure 9: Unit cell volume and the percent concentration of iron on Li sites as a function of temperature. Reproduced with permission from Chen, J.; Graetz, J. *ACS Appl. Mater. Interfaces* **2011**, *3*(5), 1380. Copyright 2011 American Chemical Society.

Studies of Doped/Partially Substituted Lithium Iron Phosphate Variants

In addition to studies of olivine materials with the Fe^{2+} cation completely substituted with other divalent metal cations (*e.g.* Mn^{2+}, Co^{2+}, Ni^{2+}),[33] research has also been conducted on doped variants of LFP. In particular, $LiFe_{1-x}Mn_xPO_4$ has garnered a lot of attention as a specimen for defect chemistry and ion transport studies.[34,35] Harrison, *et al.*[36] have been able to produce V-doped LFP using a low-temperature microwave-assisted solvothermal (MW-ST) method at $\leq$ 300 °C. Jin, *et al.*[37] cite a number of examples of $Li_3V_2(PO_4)_3$ being tested as a cathode material. Hydrothermal synthesis has also successfully produced mixed metal phosphates like $LiFe_{0.33}Mn_{0.33}Co_{0.33}PO_4$.[38] Moreover, Wang and Fan[39] recently patented a magnesium and aluminum-activated LFP cathode material, $Li_{0.9}Mg_{0.02}Al_{0.0003-0.0005}FePO_4$. The patent includes the claim that the material has an improved Li^+ intercalation/deintercalation interface environment and thus higher electronic and ionic conductivities due to the partial substitution of Mg^{2+} and Al^{3+} at the Li^+ sites.

Ternary Phase Systems with Lithium Iron Phosphate Relatives

A considerable amount of research has been dedicated to the superionic conductor $Li_3In_2(PO_4)_3$ [sodium super ion conductor (NASICON)-type structure],[40,41] including studies of ion transport mechanisms,[42] ^{7}Li and ^{31}P NMR,[43] and Li disordering.[44] Potapova, *et al.*[45,46] studied using the cross-section method the 950 °C isothermal portion of the Li_3PO_4-Na_3PO_4-$InPO_4$ ternary phase system. Samples were examined by XRD and impedance spectroscopy. Potapova, *et al.* identified five solid-solution regions based on $LiNa_5(PO_4)_2$ (*olympite* structure), In^{3+}-stabilized high temperature Na_3PO_4 [$Na_{3(1-x)}In_x(PO_4)$], $Na_3In_2(PO_4)_3$, and α- and β-$Li_3In_2(PO_4)_3$, along with a narrow melt region near eutectic equilibria (Figure 10).
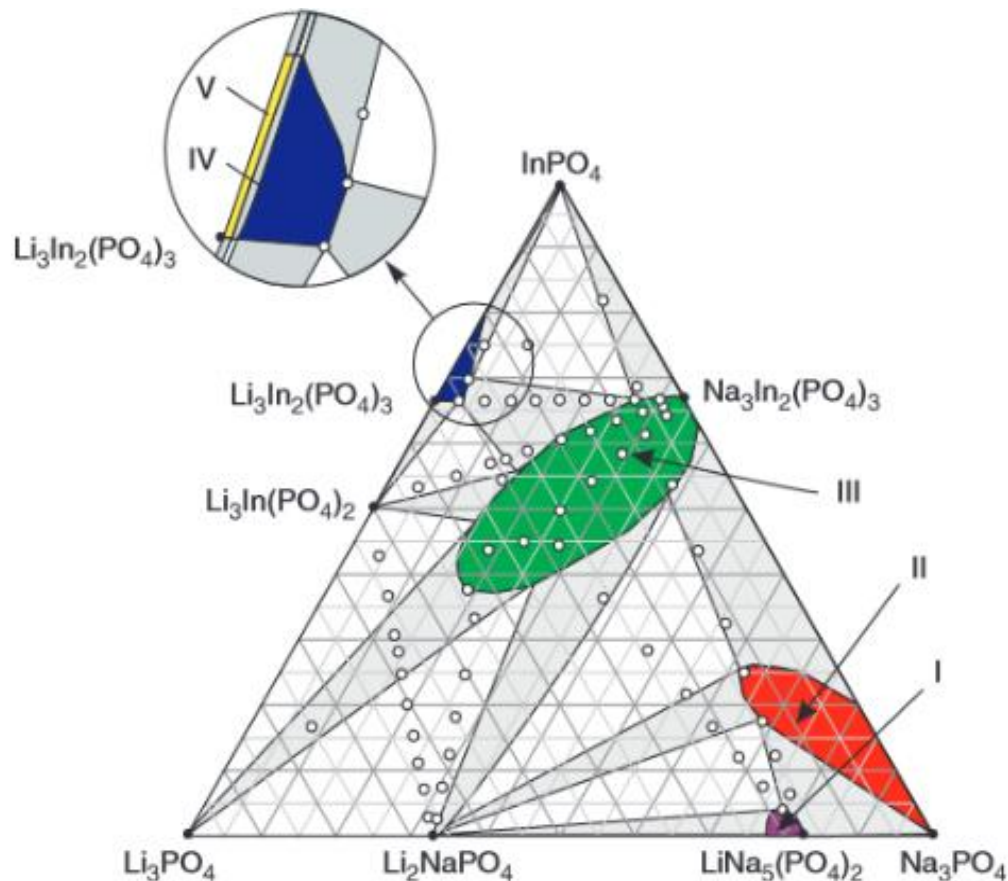
Figure 10: Phase diagram of the Li_3PO_4-Na_3PO_4-$InPO_4$ ternary system, subsolidus section at 950 °C. Homogenous fields are colored and numbered. Regions contain: (I) $LiNa_5(PO_4)_2$, (II) $Na_{3(1-x)}In_x(PO_4)$, (III) NASICON-like, high-temperature α-modification of $Na_3In_2(PO_4)_3$, (IV) low-temperature β-modification of $Li_3In_2(PO_4)_3$, and (V) NASICON-like, high-temperature α-modification of $Na_3In_2(PO_4)_3$. Reproduced with permission from Potapova, A.; Novoselov, A.; Zimina, G. *J. Am. Ceram. Soc.* **2011**, *94*(5), 1317. Copyright 2011 The American Ceramic Society.

Quaternary Compound Relatives of Lithium Iron Phosphate

Lithium iron manganese phosphates have been the subject of a number of recent studies.[47,48] Very little, however, has been published about characterizing a Li-Fe-In-(PO_4) phase. Slobodyanik, *et al.*[49] identified a pyrophosphate compound of composition $LiFe_{0.5}In_{0.5}P_2O_7$, but not a phosphate compound with composition $Li_wFe_xIn_y(PO_4)_z$, which is the target of this present study. A patent by Imaizumi, *et al.*[50] in part lists a phosphate of lithium, iron, and indium, but without a clear description of the material. Beyond these, the synthesis and structural characterization of such a phase has not been discussed.

II. EXPERIMENTAL

Synthesis

Starting Materials Summary

All products discussed herein were synthesized using solid-state reactions. Starting materials included lithium carbonate [Li_2CO_3, 99.0%, Mallinckrodt Chemicals]; isotopically-enriched lithium carbonate [$^7Li_2CO_3$, 99%, Aldrich Chemistry]; iron(II) oxalate dihydrate [$FeC_2O_4 \cdot 2H_2O$, 99%, Alfa Aesar]; indium(III) oxide [In_2O_3, 99.994%, Alfa Aesar]; ammonium phosphate monobasic [$NH_4H_2PO_4$, 98.5%, Sigma-Aldrich]; and ammonium phosphate dibasic [$(NH_4)_2HPO_4$, ScholAR Chemistry, reagent grade]. The aforementioned reagents were used without further purification.

Ceramic Method Preparation

Stoichiometric amounts of starting materials were thoroughly mixed and then ball-milled for at least 30 minutes. Following refinement of the synthetic method, these mixtures were initially heated at 350 °C for 10 hours to allow for the off-gassing of H_2O, CO_2, and NH_3 from the starting materials (refer to decomposition Equations 4 − 6); collected and reground using agate mortars and pestles; and then heated at 750 °C for 30 hours. Note that the conditions of the initial heating stage should not allow for the decomposition of Li_2CO_3. Materials were reacted in open graphite crucibles under a 95% nitrogen / 5% hydrogen (H5N) gas blend flow of approximately 7 L/h. MELLEN SV Series Split Furnaces were used to heat the reactant mixtures inside mullite tubes (Figure 11). Final products were ground using agate mortars and pestles and then transferred to glass vials for storage.

$$(4) \quad Li_2CO_3 \xrightarrow{1310\ °C} Li_2O + CO_2\uparrow$$

$$(5a) \quad 3FeC_2O_4 \cdot 2H_2O \xrightarrow{170\ °C\ -\ 230\ °C} 3FeC_2O_4 + 6H_2O\uparrow \text{ [Stage 1]}$$

$$(5b) \quad 3FeC_2O_4 \xrightarrow{230\ °C\ -\ 360\ °C} Fe_3O_4 + 4CO\uparrow + 2CO_2\uparrow \text{ [Stage 2]}$$

$$(5c) \quad 3FeC_2O_4 \cdot 2H_2O \xrightarrow{170\ °C\ -\ 360\ °C} Fe_3O_4 + 4CO\uparrow + 2CO_2\uparrow + 6H_2O\uparrow \text{ [Net]}$$

$$(6) \quad NH_4H_2PO_4 \xrightarrow{190\ °C} H_3PO_4 + NH_3\uparrow$$
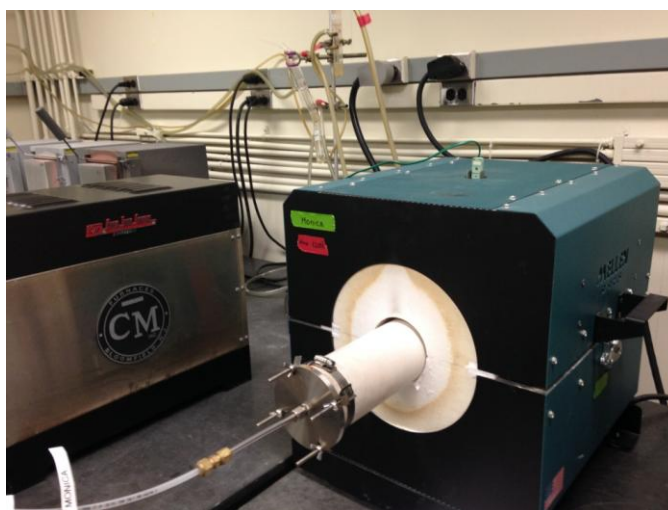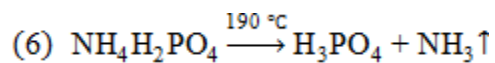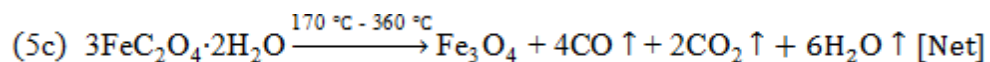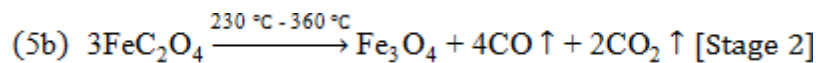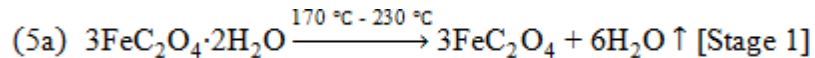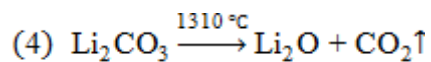
Figure 11: Example MELLEN SV Series Split Furnace used in the syntheses. H5N gas flow enters the furnace tube from the left and exits out the other end through mineral oil, seen hanging at top.
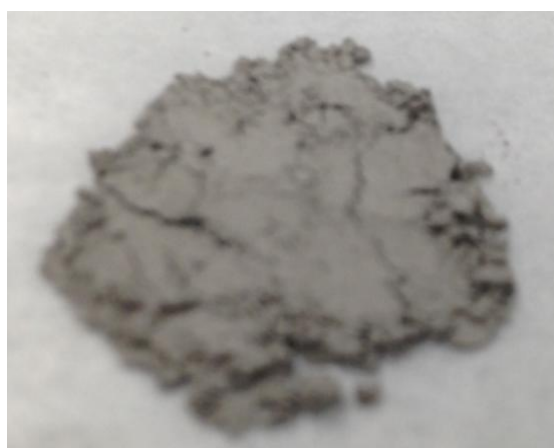
Figure 12: [7]Li-enriched LiFePO$_4$ powder sample, synthesized in an open graphite crucible under H5N at 650 °C for 40 hours, followed by an annealing period of 10 hours at 750 °C.

Figure 13: Typical LiFeIn(PO$_4$)$_2$ powder sample.

Single-Crystal Growth of Lithium Iron Indium Phosphate

Single-crystal LFIP was prepared from previously synthesized LFP and InPO$_4$. InPO$_4$ was synthesized from stoichiometric amounts of In$_2$O$_3$ and (NH$_4$)$_2$HPO$_4$, ground using a large volume quartz mortar and pestle and placed in an alumina crucible in a Thermo Scientific™ Thermolyne™ air furnace (Figure 14). This mixture was heated first at 350 °C for 10 hours and then at 900 °C for 24 hours with natural cooling to < 100 °C thereafter, a procedure modified from that used by Bosacka.[51]

In the single-crystal preparation, three mixtures were used: (1) stoichiometric amounts of the two precursors; (2) 10% molar excess of LFP; and (3) 10% molar excess of InPO$_4$. Mixture components were not ground together prior to reaction. All three mixtures were heated in open graphite crucibles in a MELLEN tube furnace under N$_2$ at 1050 °C for three hours, cooled to 750 °C over 12 hours (at a rate of 25 °C/h) and then allowed to naturally cool to < 100 °C.

Figure 14: Thermo Scientific™ Thermolyne™ air furnace used in the synthesis of InPO$_4$.

Diffraction

Routine Powder X-Ray Diffraction

A Bruker-AXS "D8 Advance" powder diffractometer [copper K$_\alpha$ radiation (40 kV, 40 mA) with a goniometer of radius 300 mm, K$_\beta$ filter, a LynxEye detector with 192 channels, a variable divergence slit of 12 mm/3˚, and a 2.5˚ primary and secondary axial Soller slit] was used to analyze the resulting products in routine measurements (Figure 15).

Figure 15: Bruker-AXS "D8 Advance" powder diffractometer used for PXRD pattern collection.

Beamline 11-BM

A pure, ^{7}Li-enriched LFIP sample was submitted for synchrotron PXRD studies at Beamline 11-BM at the Advanced Photon Source at Argonne National Laboratory. The sample was loaded and sealed with epoxy into 8-mm-diameter Kapton capillary tubes for shipment. The sample was scanned at room temperature (295.0 K) at a wavelength of 0.413708 Å.

Neutron Diffraction – Beam Line 11-A POWGEN

Isotopically-enriched samples of ^{7}Li$_{0.6}$FePO$_4$ and "^{7}Li$_{2/3}$Fe$_{2/3}$In$_{1/3}$PO$_4$" were submitted for neutron diffraction studies at Beam Line 11-A POWGEN at the Spallation Neutron Source at Oak Ridge National Laboratory. Samples were loaded into V cans and sealed with an Al lid and Cu gasket. The sample was studied at room temperature (300 K) under ambient pressure conditions. These measurements assisted in the preliminary determination of structural parameters, though they were later superseded by measurements of Li$_{2/3}$FePO$_4$ and LFIP on other instrumentation.

Electron Diffraction

An LFIP particle from a sample of "Li$_{2.5}$Fe$_{1.75}$In(PO$_4$)$_3$" product was obtained for electron diffraction patterning (EDP). Patterns were collected as the particle was tilted along an axis ([010]*) and used to construct a reciprocal lattice. From the reciprocal unit cell parameters initial parameters were determined, which were later validated by synchrotron X-ray data. Furthermore, observed reflection conditions aided in the determination of the space group to which LFIP belongs.

SEM and EDX Collection Protocol

SEM images of the as-prepared samples were collected on a JEOL 7600 SEM operating at 5 kV in a low vacuum condition to minimize charging effects. EDX spectra of the as-prepared samples were collected on a JEOL 7600 SEM operating at 15 KV equipped with an Oxford EDX spectrometer.

Battery Coin Cell Manufacture

Cathode Film Preparation

LFIP cathode films for installation in coin cells were prepared by mixing LFIP with Super P Li graphite composite and polyvinylidene fluoride copolymer in a 3:1:1 mass ratio with an agate mortar and pestle for 15 minutes. *N*-methyl-2-pyrrolidone solvent was then added, and this was ground for an additional 15 minutes to form a slurry. The slurry was spread with the pestle on a flattened surface of aluminum foil mounted on a glass plate and then placed in a Grieve forced convection bench oven (Model NB-350) operating at 100 °C to dry overnight.

Coin Cell Assembly and Cycling

Dried cathode film disks of diameter 9/16" were punched from the aluminum foil and weighed in order to calculate the specific capacity of the cathode in a tested cell. LFIP disks, battery casings, O-ring gaskets, current collectors, and springs were transferred to an argon gas glove box. Additional battery components – Li metal, electrolyte, and fiberglass separator – were already inside the glove box. The cathode material was separated from a Li metal anode (diameter 7/16") by a Whatman fiberglass disk (diameter 5/8") saturated with 1 M electrolyte solution of $LiPF_6$ in ethylene carbonate and dimethyl carbonate. The completed batteries were

sealed and then transferred out of the glove box for testing. Refer to Figure 16 for the battery cell assembly scheme.

Battery cells were allowed to rest for five hours prior to testing in order for full contact between the electrolyte and electrodes to be established. Open-circuit voltages (OCV) were measured using a voltmeter. Batteries were cycled at a rate of C/20 between 1.5 and 4.0 V for nine cycles using an Arbin Instruments BT-2000 battery testing station. Cycling data was subsequently extracted and plotted in IGOR Pro by WaveMetrics Inc.
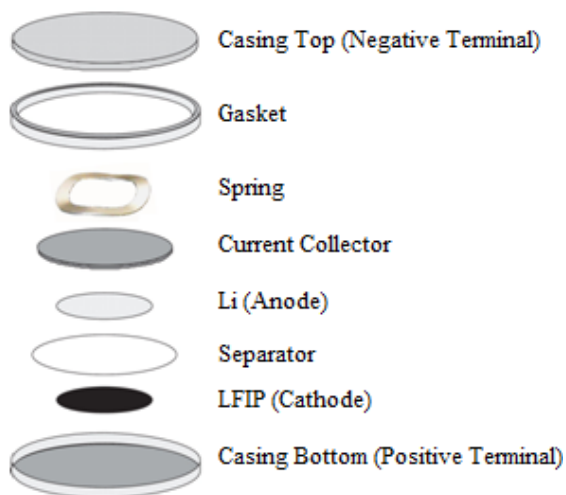
Figure 16: Assembly scheme for LFIP coin cell battery. Note that the illustration does not reflect the relative scale of the components.

III. RESULTS AND DISCUSSION

Previous Explorations and Lithium Iron Indium Phosphate Discovery

The discovery of the LFIP phase was preceded by a series of attempts to synthesize compounds belonging to the series $Li_2Fe_2M^{III}(PO_4)_3$ (equivalently, $Li_{2/3}Fe_{2/3}M^{III}_{1/3}PO_4$), where M^{III} is a trivalent cation, in an effort to produce chemical relatives of LFP with alternative charge orderings. Attempts to produce "$Li_2Fe_2Al(PO_4)_3$" (Figure 37), "$Li_2Fe_2Ga(PO_4)_3$" (Figure 38), and "$Li_2Fe_2V(PO_4)_3$" (Figure 39) failed to yield interesting results, producing mostly mixtures of LFP and $M^{III}_2O_3$.

However, the PXRD pattern of "$Li_2Fe_2In(PO_4)_3$" revealed strong novel peaks not belonging to LFP, In_2O_3, or any of a battery of plausible candidates (Figure 17). It was this intriguing finding that prompted an effort to determine the actual composition of this new phase. Through a series of attempted syntheses (Figure 18), guided by the phases observed at various data points (Table 2) within a hypothetical Li_3PO_4-$Fe_3(PO_4)_2$-$InPO_4$ compositional plot, we eventually succeeded in refining the composition of this LFIP phase to $LiFeIn(PO_4)_2$.
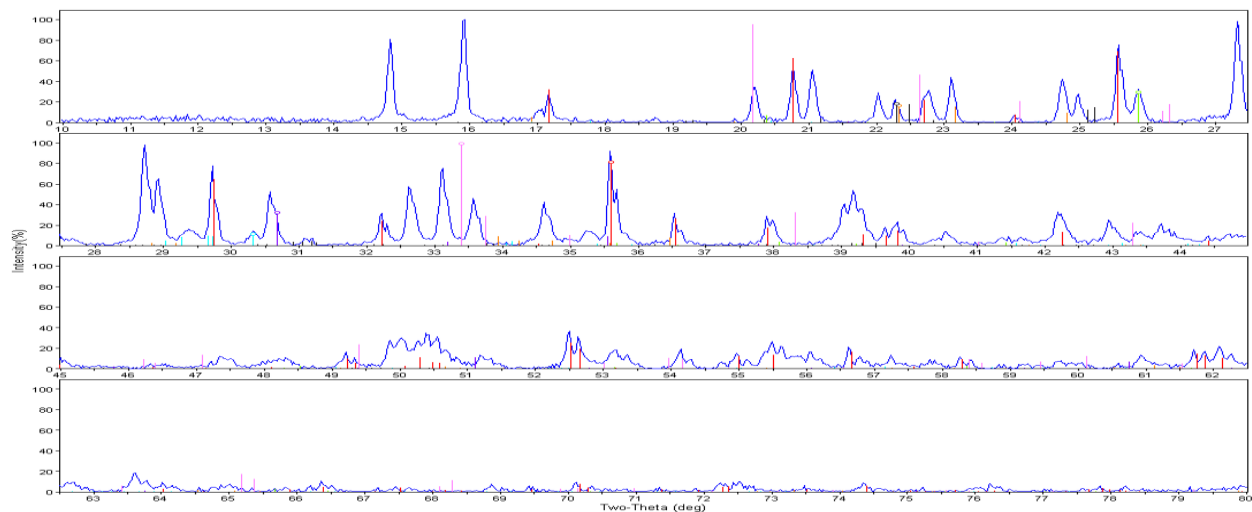
Figure 17: PXRD pattern for "$Li_2Fe_2In(PO_4)_3$" (750 °C, 8h). Shown are predicted peak positions and relative intensities for $LiFePO_4$ (red, ICDD PDF #01-074-9597), $FePO_4$ (green, #01-071-3497), In_2O_3 (purple, #01-073-6440), Li_3PO_4 (orange, #01-083-0339), $Fe_2P_2O_7$ (light blue, #01-076-1762), FeP_4O_{11} (black, #01-089-0870), and $InPO_4$ (pink, #01-072-1132).
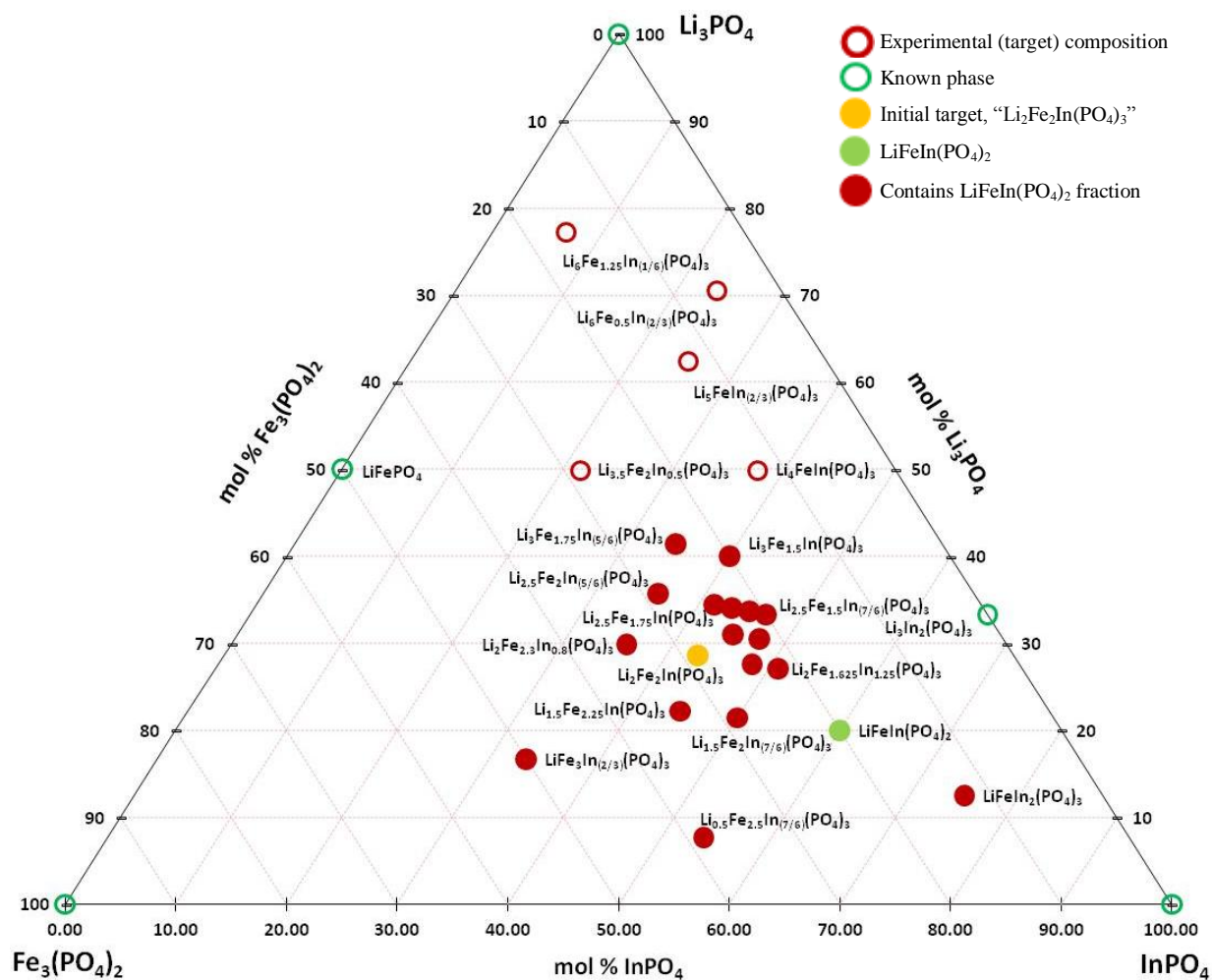
Figure 18: Experimental compositional plot.[52]

SEM Studies of Lithium Iron Phosphate and Lithium Iron Indium Phosphate

To study the phase distribution and, to a lesser extent, morphology of particles forming in the Li-Fe-In-(PO_4) solid-state solution, samples were examined by SEM. SEM images of target composition "$Li_{2.5}Fe_{1.5}In_{7/6}(PO_4)_3$" reveal at least two distinct phases (Figure 19). The major phase consists of well-faceted gray particles spanning in size from ~0.5 μm to ~3 μm in diameter and roughly spheroid in shape. The minor phase contains smaller and coarser white particles on the order of ~1 μm in diameter, also with near-round shapes. EDX measurements (*q.v.* Figure 20) revealed that the major phase corresponds to LFP and the minor phase to LFIP.
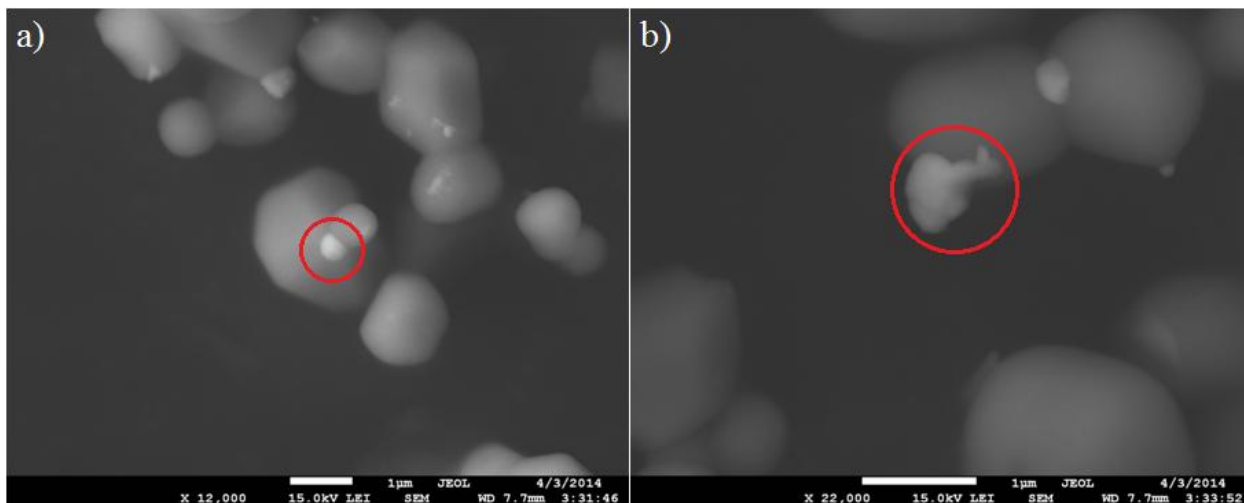
Figure 19: SEM images of a Li-Fe-In-(PO$_4$) solid-state mixture found in the "Li$_{2.5}$Fe$_{1.5}$In$_{7/6}$(PO$_4$)$_3$" sample, containing particles from at least two different phases: well-faceted gray particles (major phase), and white particles (minor phase, circled in red). Magnifications are (a) 12,000X and (b) 22,000X.

The presence of these two distinct phases refutes an earlier hypothesis that unidentified PXRD peaks which appeared in Li-Fe-In-(PO$_4$) solutions can be indexed in a 2 x 2 x 2 superstructure of LFP. Refinement of the diffraction data to fit the novel LFIP phase would further discredit this theory.

Compositional Studies of Li-Fe-In-(PO$_4$) Phase Fractions

Prior to the successful synthesis of pure LFIP, EDX spectroscopy was used to study the relative compositions of phases being observed in Li-Fe-In-(PO$_4$) solid-state solutions (Figure 20). As we have noted above, at least two types of phases were observed in target composition "Li$_{2.5}$Fe$_{1.5}$In$_{7/6}$(PO$_4$)$_3$."
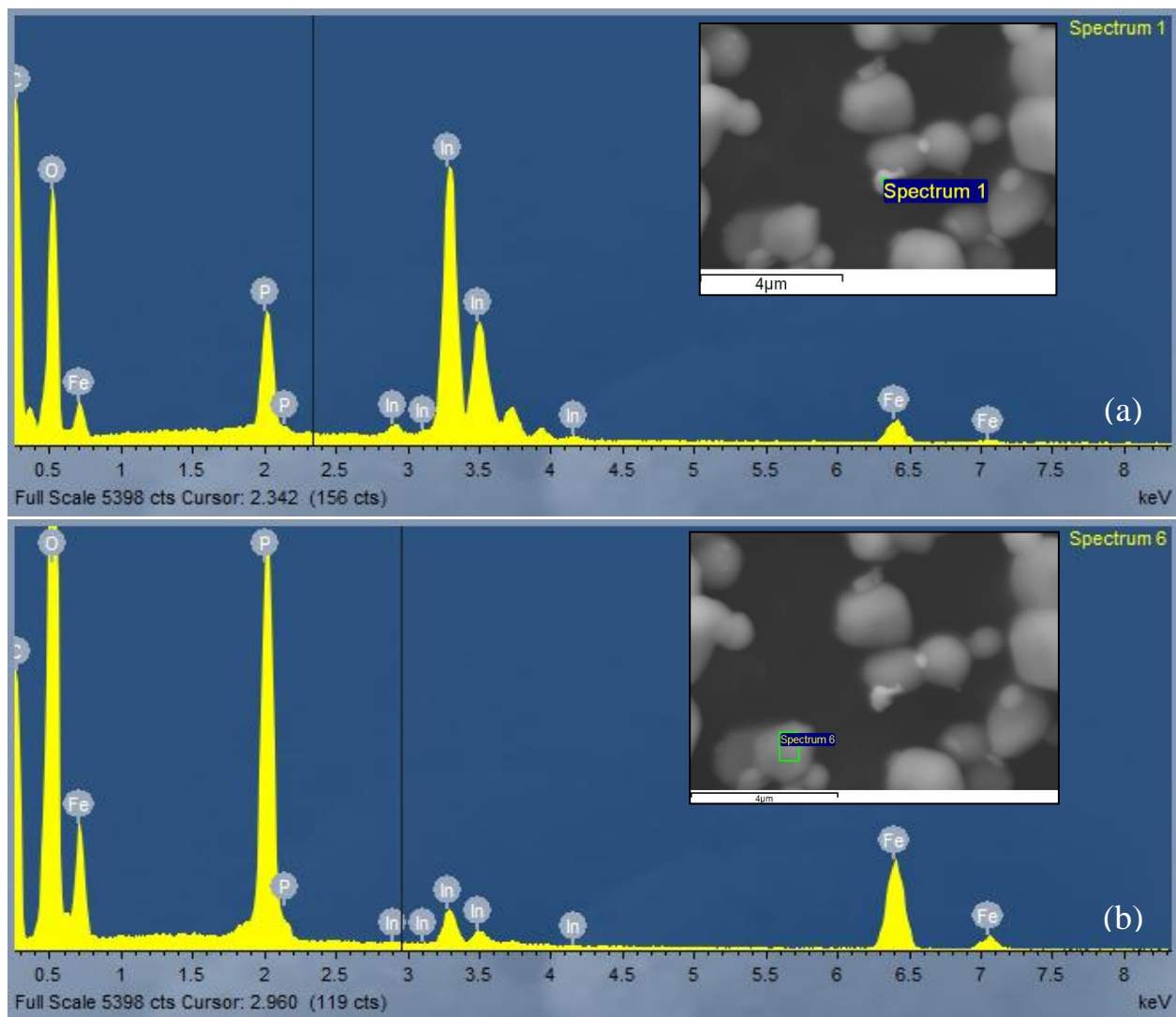
Figure 20: EDX spectra of particles found in target composition "$Li_{2.5}Fe_{1.5}In_{7/6}(PO_4)_3$" and imaged by SEM in respective insets.

As these spectra show, the white particles (Figure 20a) belong to an In-rich phase, whereas the gray particles (Figure 20b) correspond to an In-poor phase, confirming the presence of two distinct phases. The trace amounts of In observed in the second spectrum can be attributed to very small particles of the In-rich phase on the surface of the larger In-poor particle, and so In is thought to not be inherent to the composition of the larger particle. Consequently, these spectra correspond well to LFIP and LFP, respectively. As should be expected, the non-In EDX peaks scale evenly between the two phase types.

Preliminary Description of Li$_3$PO$_4$-Fe$_3$(PO$_4$)$_2$-InPO$_4$ Phase Diagram

Based on the confirmed observed phases at various data points within the Li$_3$PO$_4$-Fe$_3$(PO$_4$)$_2$-InPO$_4$ system (Table 2) we are able to propose a preliminary division of the phase system into nine triangular regions (Figure 22). We have possibly identified up to four unknown phases in addition to LFIP, (arbitrarily) designated "α," "β," "γ," and "δ." PXRD patterns (Figure 21) provide evidence suggesting the existence of these phases. These anomalous peaks fail to match LFP, LFIP, or other impurity phases known to exist in the corresponding data point's vicinity of the phase space. While many of the boundaries shown are open to validation by further synthesis attempts and phase identification, particularly those towards the right side of the diagram where there very few data points, great confidence is placed in the LFP-LFIP and LFIP-InPO$_4$ tie lines because of the phases observed at points 10, 12, and 13, each of which appears to reside on at least one of these tie lines.

We have additional evidence for the presence of the "γ" phase. EDPs of a second, In-poorer particle found in target composition "Li$_{2.5}$Fe$_{1.75}$In(PO$_4$)$_3$" determined a reciprocal lattice possibly belonging to either a C-centered monoclinic or a rhombohedral (or hexagonal) space group (Figure 40). Such a structure is not found in any of the nearby known impurities: InPO$_4$ (*Cmcm*, orthorhombic), LiFePO$_4$ (*Pnma*), Li$_3$PO$_4$ (*Pnma*), and Fe$_3$(PO$_4$)$_2$ [*P*12$_1$/c1, primitive monoclinic (both graftonite and sarcopside)]. The unit cell of this phase is similar to LFIP in parameters *a* and *b*, though it appears to have a smaller volume. It is possible for the "γ" phase to be Li$_3$In$_2$(PO$_4$)$_3$, which exists in the phase space, is rhombohedral, and close to LFIP in parameters *a* and *b*, and furthermore neatly completes the phase diagram. It does, however, have a larger unit cell volume (*a* = *b* = 8.3009 Å, *c* = 22.502 Å, *α* = *β* = 90°, *γ* = 120°, *V* = 1342.77 Å^3).[53] Further review of the EDP data will be necessary to confirm or refute this hypothesis.

Table 2: Listing of Confirmed Observed Phases at Select Data Points in the Li_3PO_4-$Fe_3(PO_4)_2$-$InPO_4$ System

Target Composition	mol % Li_3PO_4	mol % $Fe_3(PO_4)_2$	mol % $InPO_4$	Observed Phases
$Li_2Fe_2In(PO_4)_3$	28.6	28.6	42.8	$LiFePO_4$, $LiFeIn(PO_4)_2$
$Li_6Fe_{1.25}In_{1/6}(PO_4)_3$	77.4	16.1	6.5	$LiFePO_4$, Li_3PO_4, "α"
$Li_6Fe_{0.5}In_{2/3}(PO_4)_3$	70.6	5.9	23.5	Li_3PO_4, "α", "β"
$Li_{2.5}Fe_2In_{5/6}(PO_4)_3$	35.7	28.6	35.7	$LiFePO_4$, $LiFeIn(PO_4)_2$, "γ"
$Li_{2.5}Fe_{1.75}In(PO_4)_3$	34.5	24.1	41.4	$LiFePO_4$, $LiFeIn(PO_4)_2$, "γ"
$Li_2Fe_{2.3}In_{0.8}(PO_4)_3$	29.9	34.3	35.8	$LiFePO_4$, $LiFeIn(PO_4)_2$, $Fe_3(PO_4)_2$
$Li_2Fe_{1.625}In_{1.25}(PO_4)_3$	27.1	22.0	50.9	$LiFePO_4$, $LiFeIn(PO_4)_2$, "γ"
$Li_{1.5}Fe_{2.25}In(PO_4)_3$	22.2	33.3	44.5	$LiFePO_4$, $LiFeIn(PO_4)_2$, $Fe_3(PO_4)_2$
$Li_{1.5}Fe_2In_{7/6}(PO_4)_3$	21.4	28.6	50.0	$LiFePO_4$, $LiFeIn(PO_4)_2$, $Fe_3(PO_4)_2$
$LiFe_3In_{2/3}(PO_4)_3$	16.7	50.0	33.3	$Fe_3(PO_4)_2$, $LiFeIn(PO_4)_2$, $LiFePO_4$
$LiFeIn_2(PO_4)_3$	12.5	12.5	75.0	$InPO_4$, $LiFeIn(PO_4)_2$
$Li_{0.5}Fe_{2.5}In_{7/6}(PO_4)_3$	7.7	38.5	53.8	$Fe_3(PO_4)_2$, "δ", $LiFeIn(PO_4)_2$
$Li_{1.5}Fe_{1.5}In_{1.5}(PO_4)_3$	20.0	20.0	60.0	$LiFeIn(PO_4)_2$
$Li_{3.5}Fe_2In_{0.5}(PO_4)_3$	50.0	28.6	21.4	$LiFePO_4$, "α", Li_3PO_4
$Li_4FeIn(PO_4)_3$	50.0	12.5	37.5	Li_3PO_4, "α", "β"
$Li_5FeIn_{2/3}(PO_4)_3$	62.5	12.5	25.0	Li_3PO_4, "α", "β"
$Li_3Fe_{1.75}In_{5/6}(PO_4)_3$	41.4	24.1	34.5	$LiFePO_4$, $LiFeIn(PO_4)_2$, "γ"
$Li_3Fe_{1.5}In(PO_4)_3$	40.0	20.0	40.0	$LiFePO_4$, $LiFeIn(PO_4)_2$, "γ"
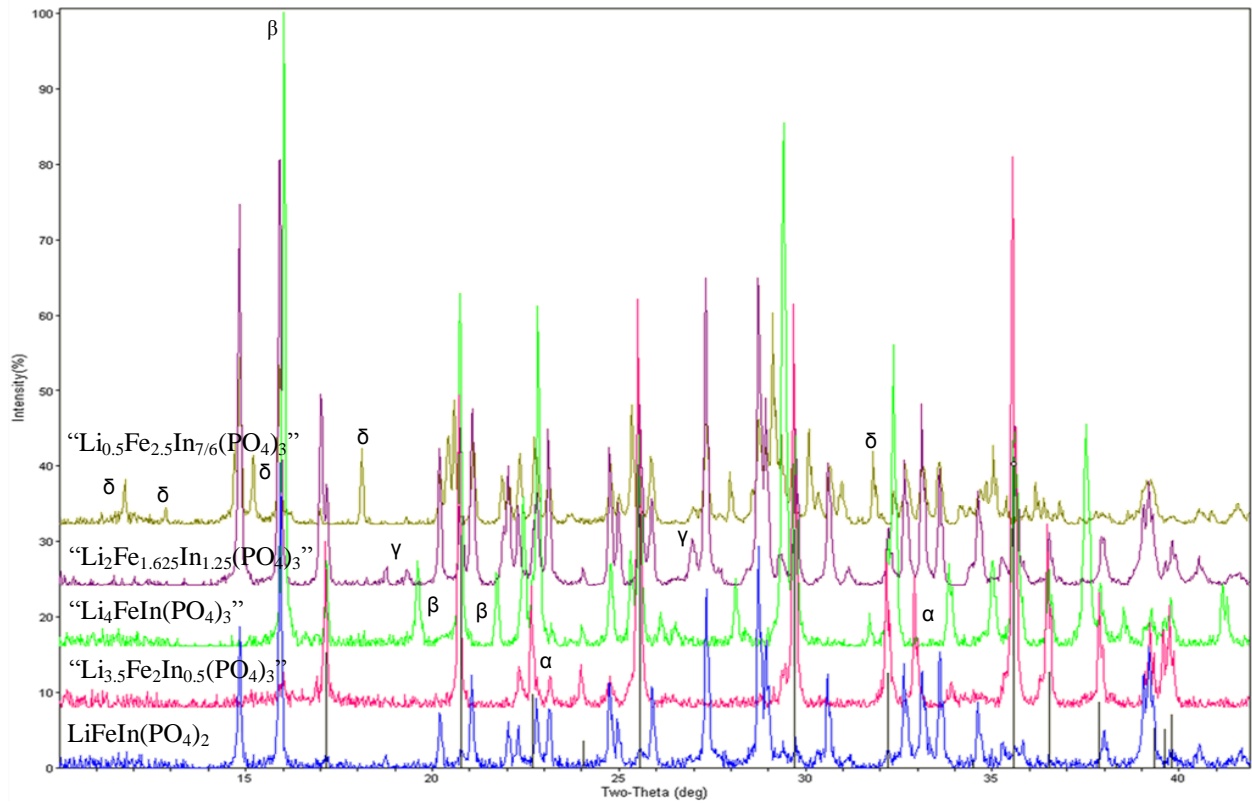
Figure 21: PXRD patterns of $LiFeIn(PO_4)_2$ and "$Li_xFe_yIn_z(PO_4)_3$" test samples with unidentified peaks marked by Greek letter of arbitrary phase name. $LiFePO_4$ peak positions and relative intensities are marked at bottom (ICDD PDF #01-083-2092).
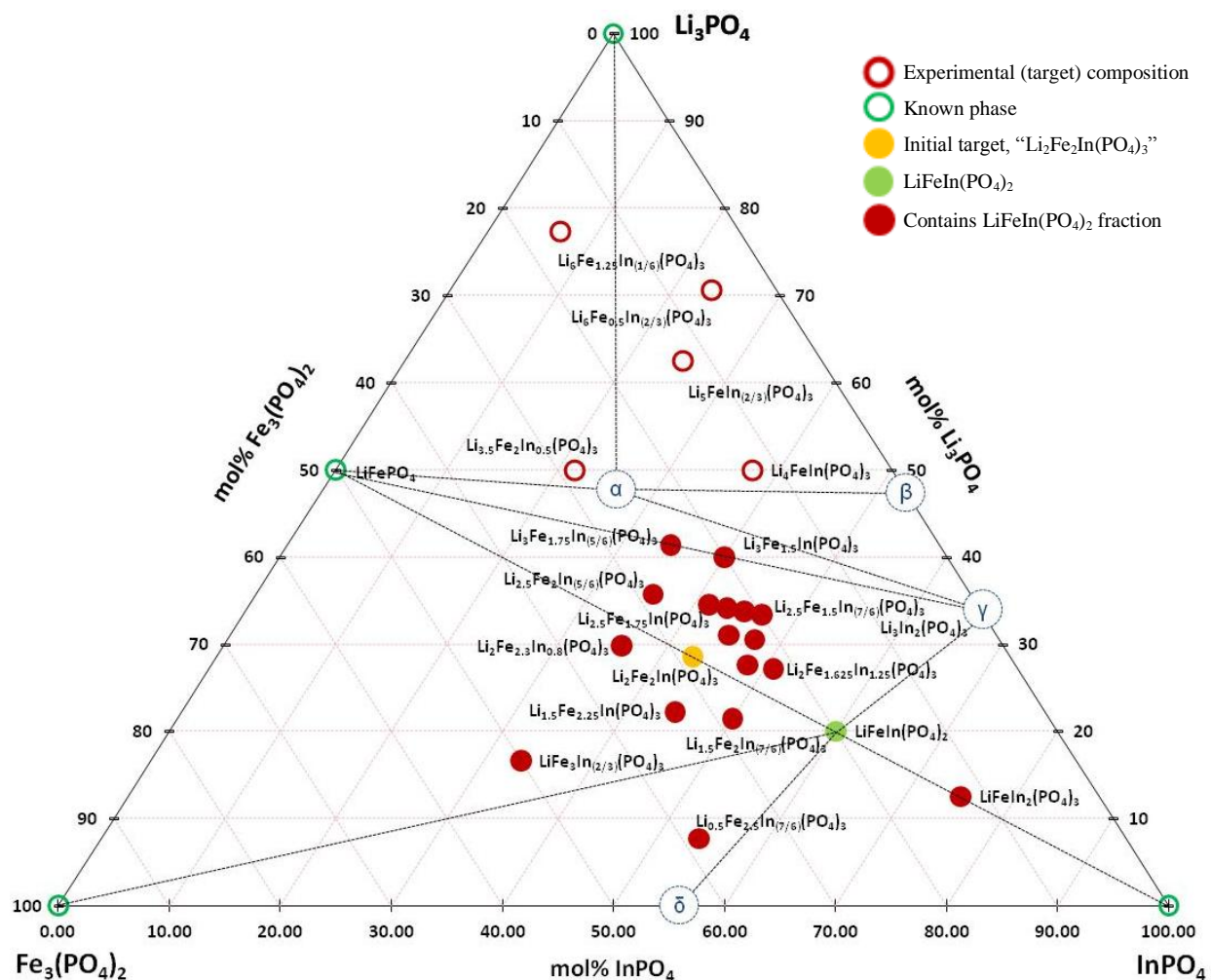
Figure 22: Preliminary proposed division of Li_3PO_4-$Fe_3(PO_4)_2$-$InPO_4$ phase system into triangular regions.

Structure Determination of Lithium Iron Indium Phosphate

PXRD patterns collected by the D8 Advance diffractometer were initially studied with MDI Jade 9 software by Materials Data, Inc. to compare against those of previous syntheses and database patterns as well as determine lattice parameters. Rietveld refinements of patterns were carried out by combined utilization of four software programs: TOPAS (Version 4.2, Bruker AXS), Jana2006 (Version 06/11/2013), and WinPLOTR and DICVOL within the FullProf Suite of programs (Version July-2011, JGP - JRC).

Successful solution of the crystal structure of LFIP required firstly the synthesis of a pure phase. After numerous attempts at refining the novel phase's composition, we succeeded in producing a single-phase sample of LFIP (Figure 23), devoid of even the tenacious LFP phase.
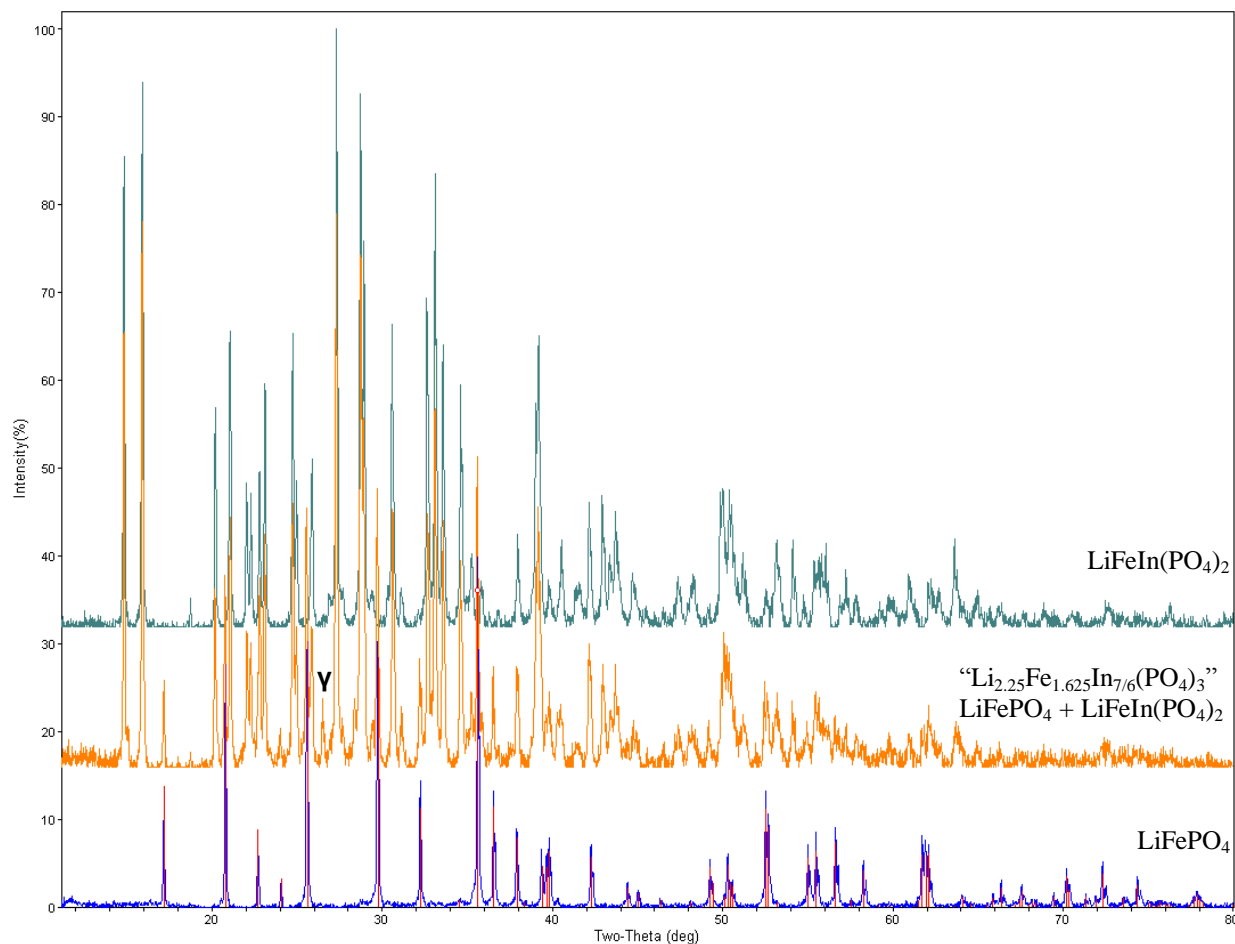
Figure 23: Illustration of differences in PXRD patterns between $LiFePO_4$, a $LiFeIn(PO_4)_2$ test composition ("$Li_{2.25}Fe_{1.625}In_{7/6}(PO_4)_3$"), and single-phase $LiFeIn(PO_4)_2$. Gamma ("γ") indicates a peak perhaps belonging to another unidentified phase or composition within the phase space; please see "Conclusions and Future Prospects." Typical $LiFePO_4$ phase peak positions are indicated by tick marks along the abscissa (ICDD PDF #01-083-2092).

EDPs of an LFIP particle from target composition "$Li_{2.5}Fe_{1.75}In(PO_4)_3$" had previously been taken and greatly helped in establishing possible space groups to which LFIP might belong as well as initial cell parameters (Figure 24). The reciprocal lattice is a primitive orthorhombic lattice with $a* = 0.723$ nm^{-1}, $b* = 1.05$ nm^{-1}, and $c* = 1.08$ nm^{-1}, corresponding to a lattice with $a = 13.8$ Å, $b = 9.5$ Å, and $c = 9.3$ Å. Moreover, the reflection condition h = 2n for the hk0 plane is

observed. This indicates the presence of an *a* glide in the *a-b* plane (perpendicular to the *c* axis), further limiting the list of candidate space groups.
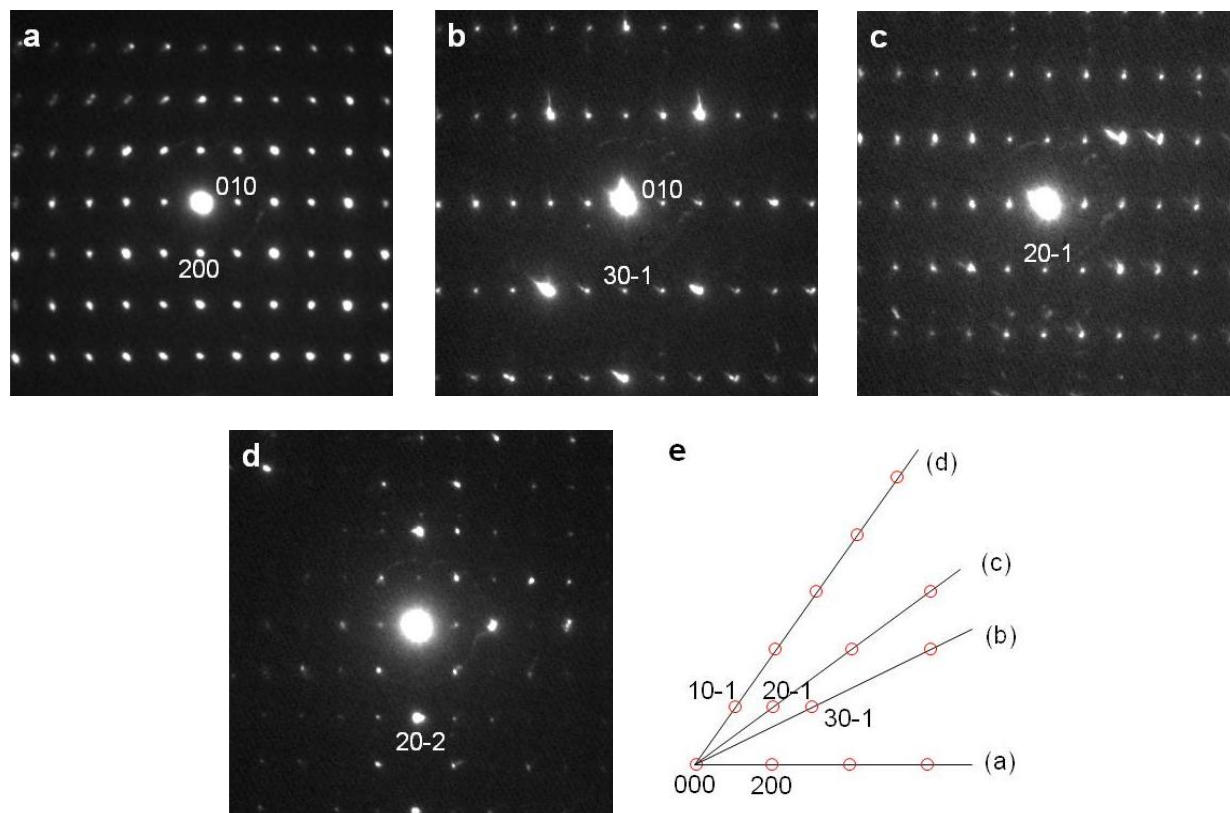
Figure 24: (a-e) EDPs from a LiFeIn(PO$_4$)$_2$ particle measured by tilting the particle along axis [010]*. The tilting angles from (a) to (b), (c), and (d) are 26.2°, 36.6° and 55.0°, respectively. (e) Reconstructed reciprocal plane perpendicular to the tilting axis. We observe the general reflection condition h = 2n for the hk0 plane from (a).

Refinement of the LFIP crystal structure from single-crystal data (Figure 25) determined that the phase is primitive orthorhombic, *Pbca* (No. 61), *a* = 9.276(1) Å, *b* = 13.757(2) Å, *c* = 9.476(1) Å, *V* = 1209.13(1) Å^3 (molar mass = 367.5467 g·mol^{-1}). This space group has a unique set of reflection conditions (and systematic absences), making identification of the space group and pattern indexing definitive. Prominent features of *Pbca* include three glide planes − one perpendicular to each axis − and the consequent three two-fold screw axes. This space group does not contain mirror planes. The atomic site positions and isotropic displacement parameters

(U_{eq}) (Table 3) and anisotropic displacement parameters (Table 4) for LFIP are given below. Bond lengths (Table 5) and angles (Table 9) are also provided.
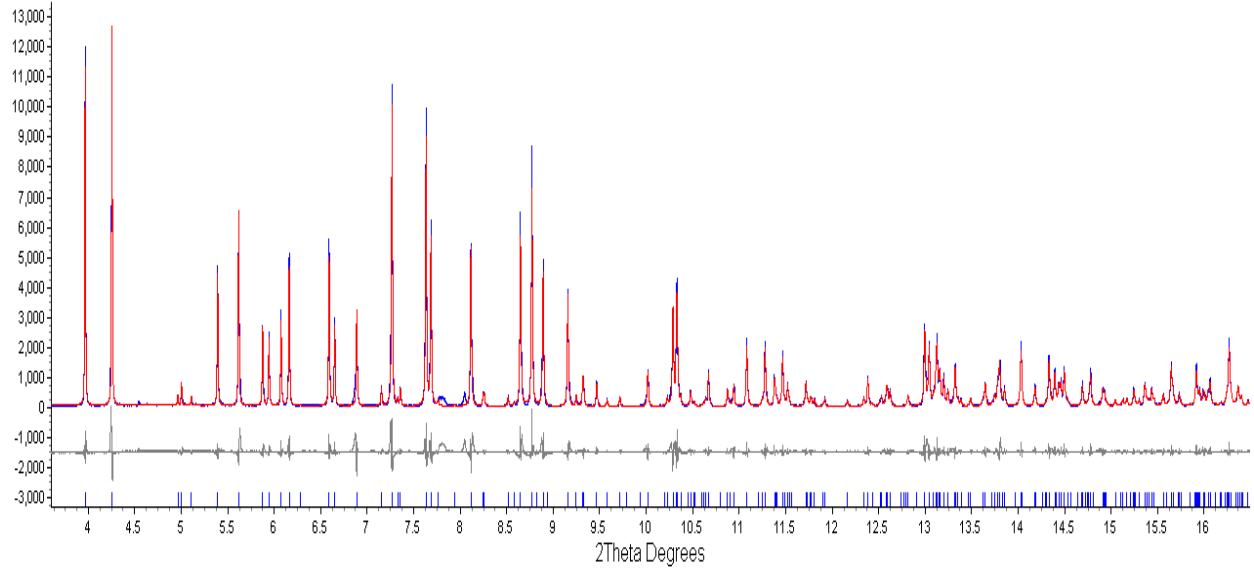
Figure 25: PXRD pattern from synchrotron data with *Pbca* Rietveld refinement of LiFeIn(PO$_4$)$_2$.

Table 3: Standardized Atomic Site Positions and Isotropic Displacement Parameters (U_{eq}) in LiFeIn(PO$_4$)$_2$ as Refined from Single-Crystal Data (*Pbca*)

Site	x	y	z	U_{eq} (Å^2)
Li	0.0498(4)	0.1298(2)	0.2804(4)	0.0138(8)
Fe	0.27980(3)	0.12226(2)	0.03402(3)	0.00990(6)
In	0.39972(1)	0.377090(7)	0.14168(1)	0.00614(4)
P1	0.06788(4)	0.27304(3)	0.07430(4)	0.00594(8)
P2	0.31586(4)	0.01242(3)	0.33422(4)	0.00617(8)
O1	0.49635(1)	0.15179(9)	0.02085(1)	0.0098(3)
O2	0.00974(1)	0.27597(8)	0.22513(1)	0.0106(3)
O3	0.02666(1)	0.49991(8)	0.29124(1)	0.0103(3)
O4	0.04219(1)	0.16742(8)	0.02107(1)	0.0092(2)
O5	0.23520(1)	0.27761(8)	0.0714(1)	0.0098(2)
O6	0.2529(1)	0.09721(8)	0.2523(1)	0.0090(2)
O7	0.2656(1)	0.41510(8)	0.3109(1)	0.0089(2)
O8	0.2989(1)	0.02314(8)	0.4962(1)	0.0093(2)

Table 4: Anisotropic Displacement Parameters in LiFeIn(PO$_4$)$_2$ as Refined from Single-Crystal Data

Site	U_{11} (Å^2)	U_{22} (Å^2)	U_{33} (Å^2)	U_{12} (Å^2)	U_{13} (Å^2)	U_{23} (Å^2)
Li	0.013(1)	0.014(1)	0.015(1)	0.0020(9)	0.002(1)	-0.001(1)
Fe	0.0101(1)	0.0100(1)	0.0097(1)	-0.00151(6)	0.00030(7)	-0.00083(6)
In	0.00592(6)	0.00649(6)	0.00601(6)	0.00045(3)	0.00027(3)	-0.00026(2)
P1	0.0056(1)	0.0060(1)	0.0062(1)	0.0001(1)	-0.0001(1)	-0.0004(1)
P2	0.0059(1)	0.0063(1)	0.0063(1)	0.0000(1)	-0.0007(1)	-0.0000(1)
O1	0.0092(4)	0.0101(5)	0.0100(4)	-0.0024(3)	-0.0004(3)	-0.0027(3)
O2	0.0138(4)	0.0112(4)	0.0069(4)	0.0028(4)	0.0029(4)	-0.0003(3)
O3	0.0067(4)	0.0098(4)	0.0142(5)	-0.0014(3)	-0.0014(3)	0.0013(4)
O4	0.0108(4)	0.0065(4)	0.0104(4)	-0.0007(3)	-0.0027(3)	-0.0018(3)
O5	0.0063(4)	0.0090(4)	0.0141(5)	-0.0008(3)	-0.0009(3)	-0.0008(3)
O6	0.0089(4)	0.0102(4)	0.0081(4)	0.0022(4)	-0.0008(3)	0.0022(3)
O7	0.0110(4)	0.0076(4)	0.0081(4)	0.0029(3)	0.0023(3)	0.0000(3)
O8	0.0127(4)	0.0085(4)	0.0065(4)	-0.0020(3)	-0.0007(3)	-0.0007(3)

Table 5: Bond Distances in LFIP as Refined from Single-Crystal Data

Atom 1	Atom 2	Bond Distance (Å)	Atom 1	Atom 2	Bond Distance (Å)
Li	O6	1.955(4)	In	O2	2.138(1)
Li	O1	1.971(4)	In	O3	2.155(1)
Li	O3	2.038(3)	In	O5	2.155(1)
Li	O2	2.111(3)	In	O8	2.159(1)
Fe	O1	2.053(1)	P1	O1	1.524(1)
Fe	O6	2.112(1)	P1	O2	1.528(1)
Fe	O8	2.159(1)	P1	O5	1.554(1)
Fe	O7	2.180(1)	P1	O4	1.557(1)
Fe	O5	2.205(1)	P2	O6	1.518(1)
Fe	O4	2.293(1)	P2	O3	1.526(1)
In	O7	2.095(1)	P2	O8	1.550(1)
In	O4	2.121(1)	P2	O7	1.553(1)

The crystal structure of LFIP (Figure 26) contains eight atomic sites: one Li site, one Fe site, one In site, two P sites, and eight O sites. Its atoms are arranged in assorted polyhedra which are not directly connected to one another: distorted LiO$_4$ tetrahedra, distorted FeO$_6$ octahedra, InO$_6$ octahedra, and PO$_4$ tetrahedra (Figure 27). Each LiO$_4$ tetrahedron shares two of its vertices with an FeO$_6$ octahedron and a PO$_4$ tetrahedron; it shares its two remaining vertices with an InO$_6$ octahedron and a PO$_4$ tetrahedron (Figure 28a). Each FeO$_6$ octahedron shares its two shortest edges with PO$_4$ tetrahedra. The FeO$_6$ octahedra share at each of the four vertices forming these edges a corner with an InO$_6$ octahedron; it shares each of its remaining two with a LiO$_4$

31

tetrahedron and a PO_4 tetrahedron (Figure 28b). At four of its vertices, each InO_6 octahedron shares a vertex with a PO_4 tetrahedron and a FeO_6 octahedron; at each of its remaining two vertices it shares corners with a LiO_4 tetrahedron and a PO_4 tetrahedron (Figure 28c).

(a)

(b)

(c)
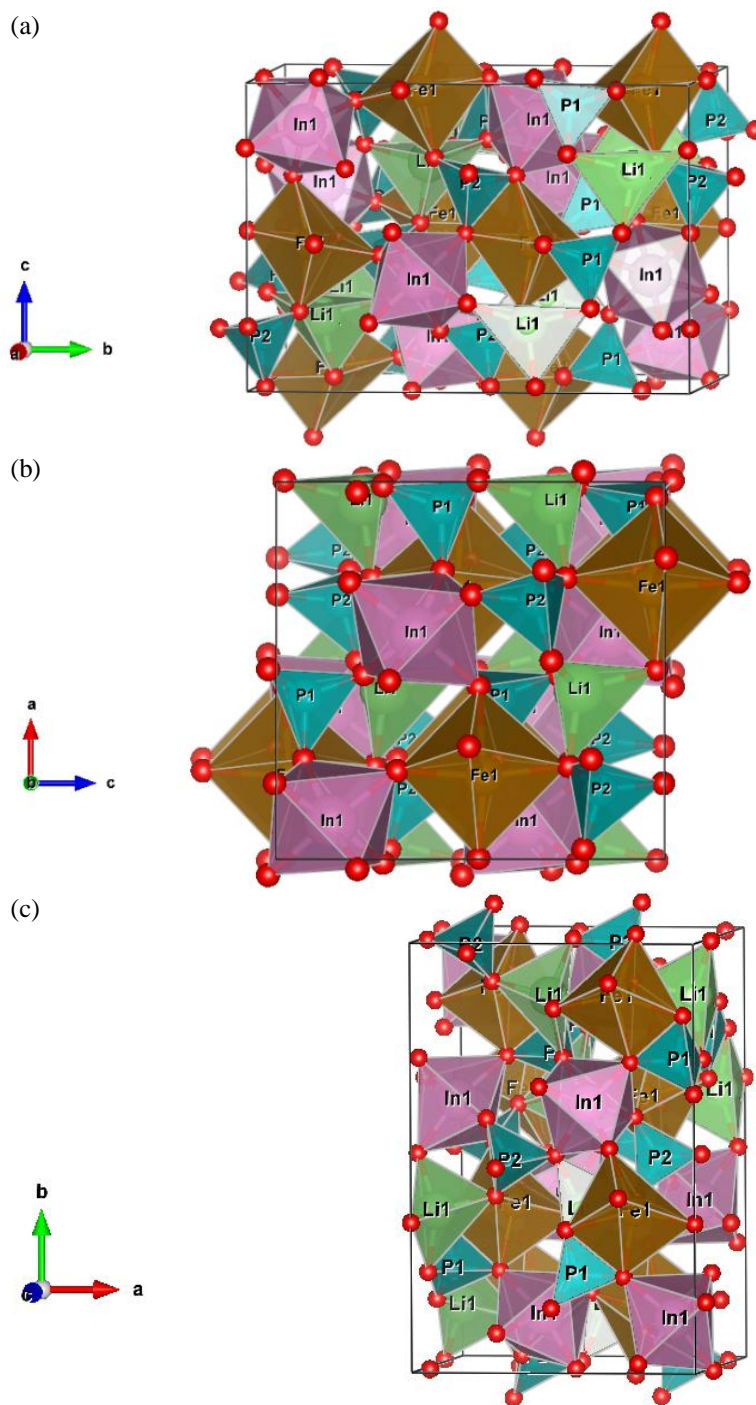
Figure 26: Crystal structure of $LiFeIn(PO_4)_2$ as viewed along the (a) approximate *a*, (b) *b*, and (c) approximate *c* directions. O site labels have been omitted for clarity.
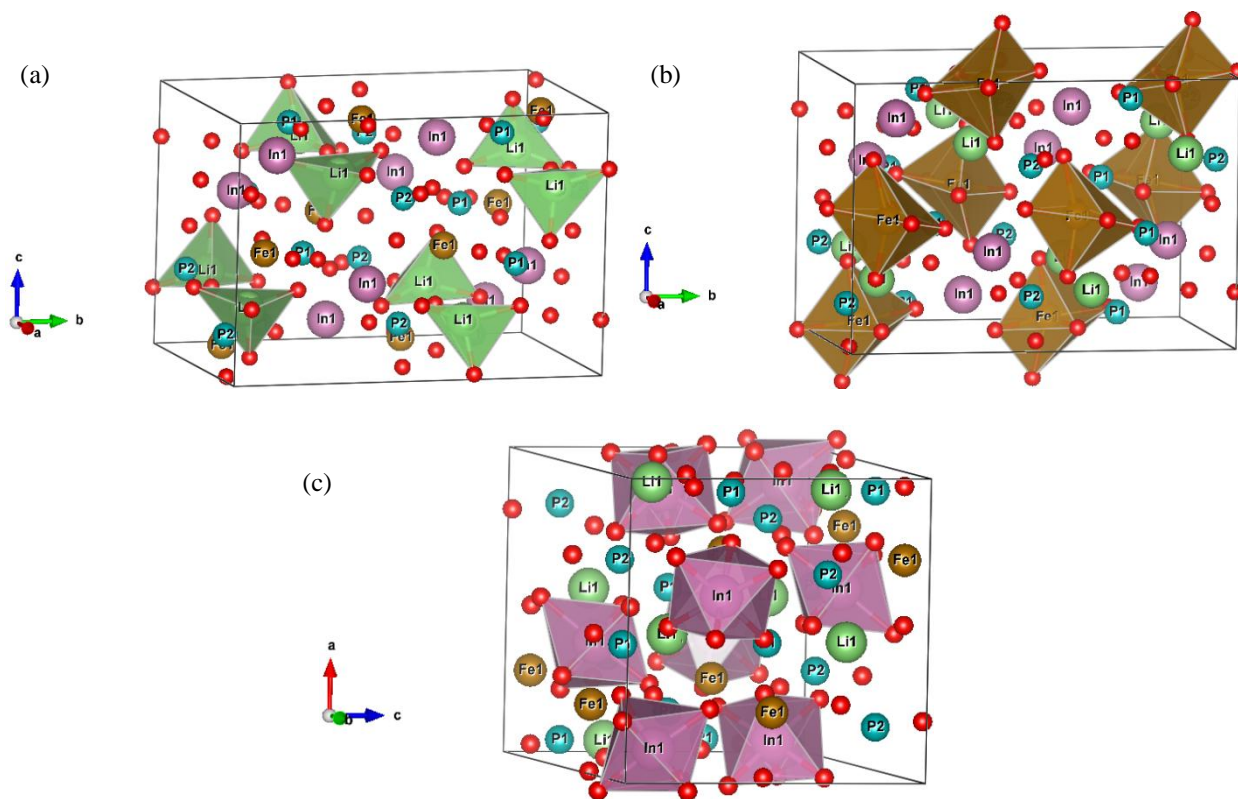
Figure 27: Illustration showing disconnect between like polyhedra: (a) LiO_4, (b) FeO_6, and (c) InO_6.
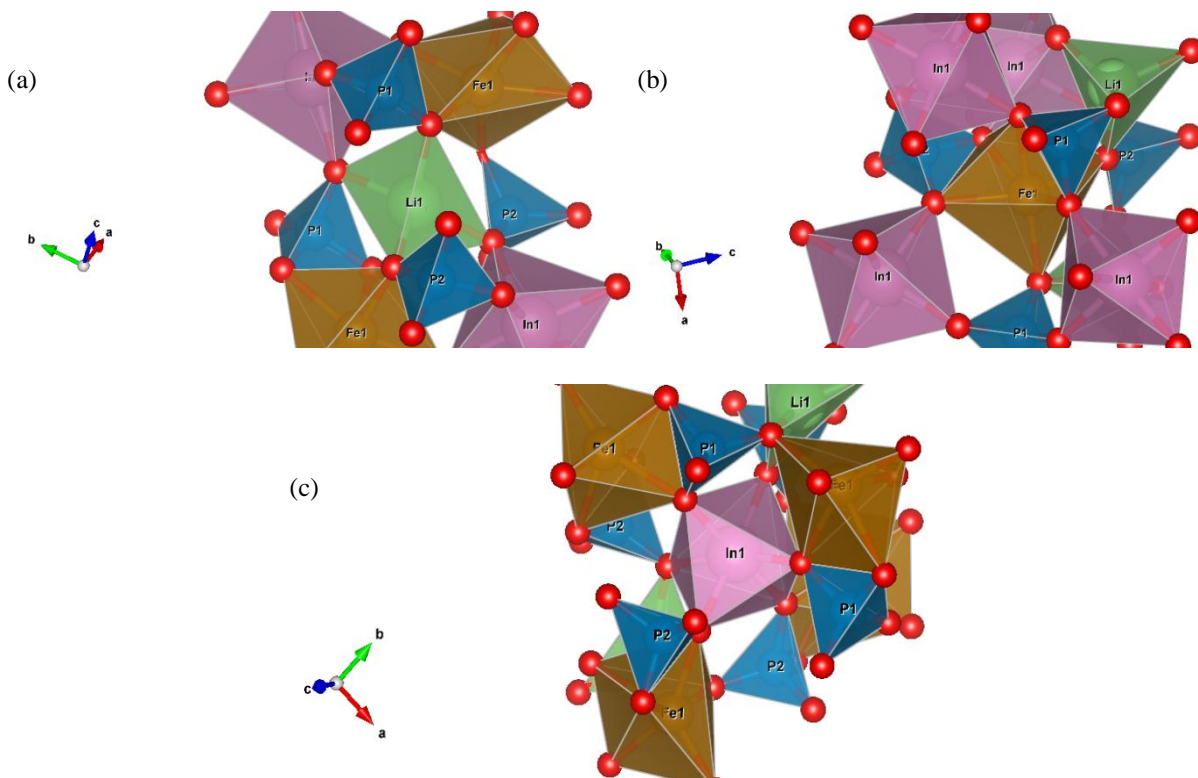
Figure 28: Local environments of the (a) LiO_4, (b) FeO_6, and (c) InO_6 polyhedra. Nearest neighbors are shown.

33

In an effort to identify other phosphates with the same structure prototype, a search of Pearson's Crystal Data[54] failed to yield any such results. However, a broader search beyond phosphate compounds showed that the present structure's prototype is exhibited in orthorhombic $Li_2Ni(SO_4)_2$, as determined by Isasi, *et al.*[55] Hits in this search were required to satisfy the following criteria: 1) the structure belongs to space group *Pbca*, 2) it contains at least one functional group of the form XO_4 (X = As, Cl, Cr, Ge, Mo, N, P, Re, Se, Si, S, V, W), 3) it contains at least one alkali metal (Li, Na, K, Rb, Cs, Fr), and 4) it contains between 4 and 10 (types of) elements. An extended list of initial hits in the database is divided between Table 10 and Table 11 under "Supplementary Figures and Tables." Hits were separated based on strength of candidacy, wherein hits whose chemical formulas fail to fit the three-cation, two-polyatomic-anion chemical formula template by a discrepancy of one cationic or anionic unit or greater (following normalization of the formula) were considered poor candidates for structural similarity to LFIP. It is worth noting the similarities in cell parameters and analogous element ratios between entries "$Li_2Mn_2(SO_4)_3$" and "$Li_{3.56}(PO_4)_6Ti_4 \sim Li_2Ti_2(PO_4)_3$;" however, their structures are distinct from that of $Li_2Ni(SO_4)_2$.

The $Li_2Ni(SO_4)_2$ structure prototype is unlike that of its cobalt, iron,[56] and manganese[57] chemical analogues [*marinite*, $Li_2M(SO_4)_2$, M = Co, Fe, Mn], which crystallize in the monoclinic space group $P2_1/c$. These *marinite* structures lack the (distorted) LiO_6 octahedra present in $Li_2Ni(SO_4)_2$. In the orthorhombic structure (Figure 29), isolated NiO_6 octahedra share at each vertex a common oxygen linkage to one LiO_6 octahedron and one SO_4 tetrahedron. The LiO_6 octahedra share edges with two SO_4 tetrahedra. By contrast, in the *marinite* structure (Figure 30) the independent MO_6 octahedra are linked through common oxygen vertices with SO_4 tetrahedra. Each octahedron is connected to six SO_4 tetrahedra which form a "pinwheel" configuration when

viewed along the a axis. However, each tetrahedron is linked to only three MO_6 octahedra; the fourth vertex of the tetrahedra points into an open Li ion channel. Reynaud and coworkers[58] also studied the magnetic structure of $Li_2Ni(SO_4)_2$. A search of the literature has failed to yield a name for the orthorhombic prototype.
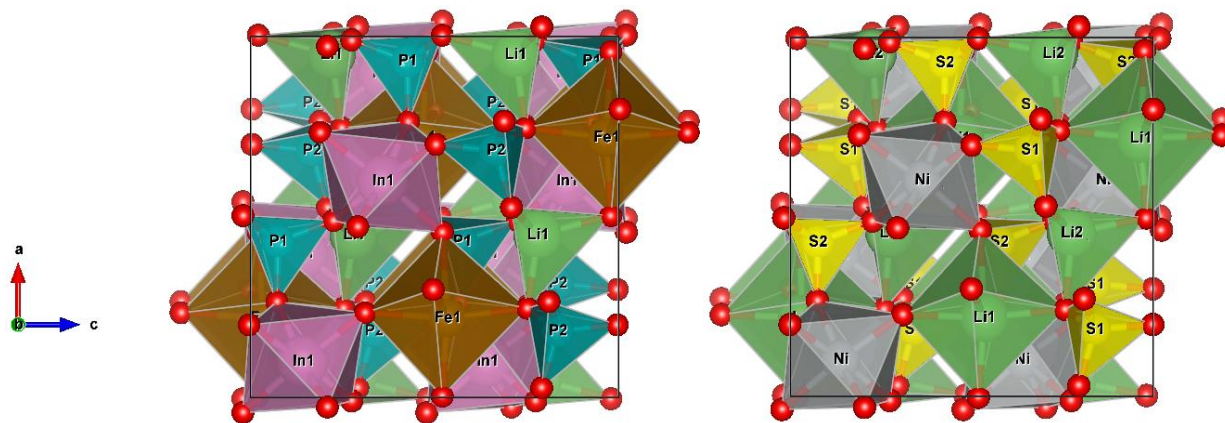
Figure 29: Crystal structures of $LiFeIn(PO_4)_2$ (left) and $Li_2Ni(SO_4)_2$ (right) viewed along the b direction.[55]
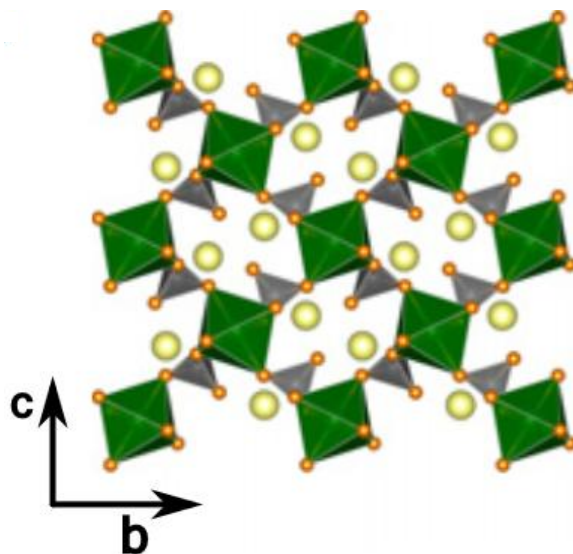
Figure 30: Representative illustration of the competing *marinite* crystal structure in $Li_2Fe(SO_4)_2$ viewed along the a direction. Reproduced with permission from Reynaud, M.; Ati, M.; Melot, B. C.; Sougrati, M. T.; Rousse, G.; Chotard, J.-N.; Tarascon, J.-M. *Electrochem. Commun.* **2012**, *21*, 77. Copyright 2012.

The analogous atoms of $Li_2Ni(SO_4)_2$ were identified by the geometries exhibited in their crystal structures (*q.v.* Figure 29). The tetrahedral Li site in $Li_2Ni(SO_4)_2$ corresponds to the tetrahedral Li site in LFIP, whereas the octahedral Li site corresponds to the octahedral Fe site in LFIP, the octahedral Ni site to the octahedral In site, and the tetrahedral S sites to the tetrahedral P sites. The corresponding O sites were also successfully identified (Table 6).

Table 6: Analogous Atomic Sites between $LiFeIn(PO_4)_2$ and $Li_2Ni(SO_4)_2$

LFIP	Li	Fe	In	P1	P2	O1	O2	O3	O4	O5	O6	O7	O8
$Li_2Ni(SO_4)_2$	Li2	Li1	Ni	S2	S1	O21	O24	O12	O22	O23	O14	O13	O11

A search of the literature has found recent work by Lander, *et al.*[59] claiming that no electrochemical activity was observed in $Li_2Ni(SO_4)_2$ when cycled between 3.0 V and 4.5 V *vs.* Li^+/Li at a C-rate of C/20. It is possible, then, given its structural resemblance, that LFIP may perform similarly. Additionally, Reynaud, *et al.*[60] conducted studies on the magnetic structure and properties of $Li_2Ni(SO_4)_2$ – found to be antiferromagnetic – but it is inappropriate to draw parallels to LFIP due to differences in magnetic elements.

Magnetic Measurements of Lithium Iron Indium Phosphate

The magnetic properties of LFIP were studied by measuring the magnetization between 2 K and 350 K of a powder sample in an applied magnetic field of 0.1 T (Figure 31). The absence of anomalies in the temperature-dependent magnetization reveals that the material does not order magnetically above the base temperature of 2 K. The effective magnetic moment for Fe^{2+} in LFIP was determined from temperature-dependent magnetic susceptibility, as determined from the temperature-dependent magnetization. The magnetism in the material obeys the Curie-Weiss law $\left(\chi = \frac{C}{T+\theta}\right)$. The inverse susceptibility χ^{-1} is linear between ~30 K and 350 K, which leads to

an effective magnetic moment of 5.39 μ_B/Fe, and the constant θ equals -9.5 K, indicating weak antiferromagnetic interactions.
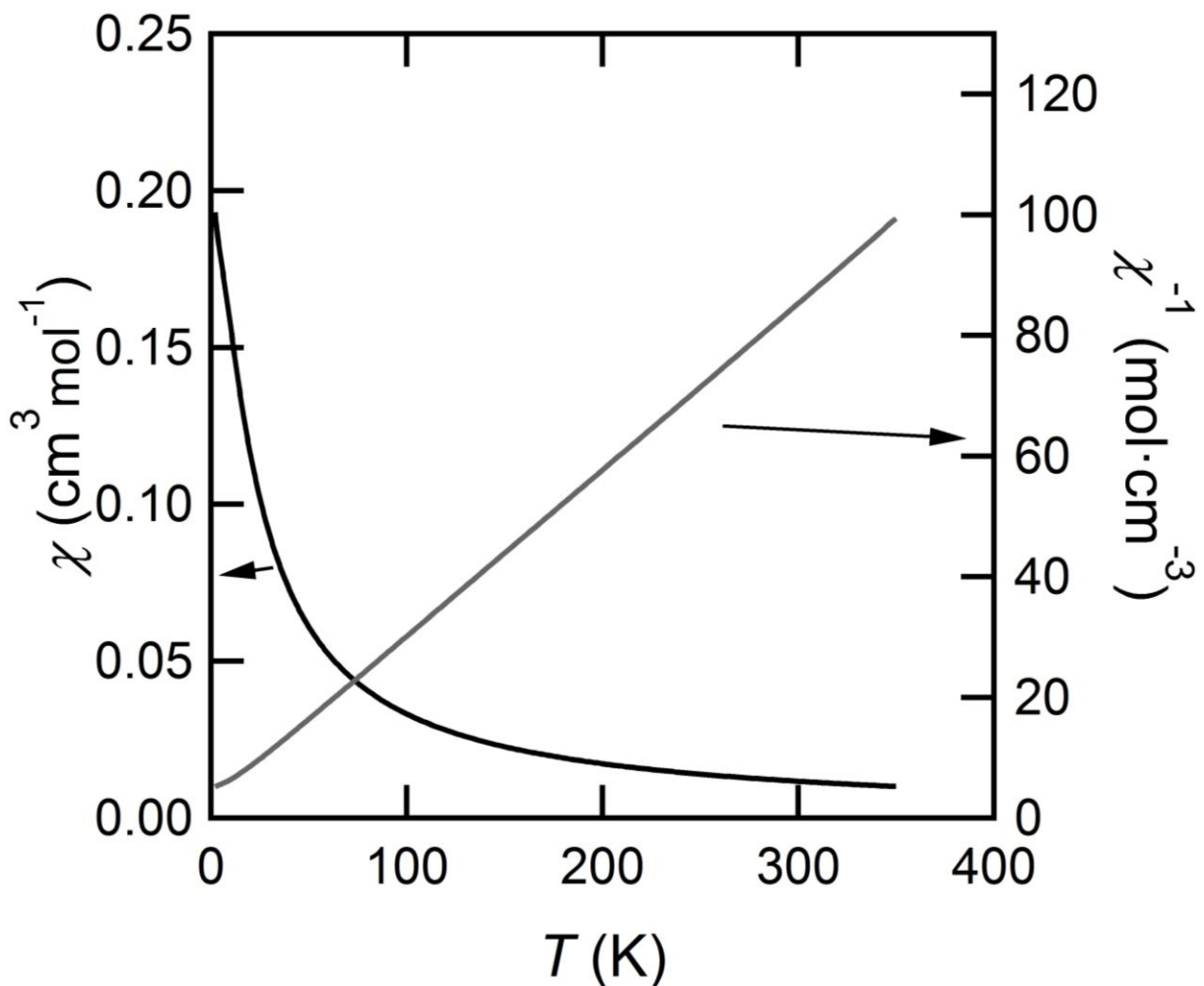
Figure 31: Magnetic measurements of LFIP. Arrows indicate to which ordinate axis each curve corresponds.

These results can be rationalized by the structural environment of the FeO_6 octahedra. As stated above, these octahedra are isolated and therefore are unlikely to give rise to magnetic exchange. The d electrons in Fe^{2+} lack exchange pathways that could give rise to strong spin coupling, although it is possible that the exchange interaction for magnetic ordering can be via the oxygen coordination. Additionally, In^{3+} cannot significantly contribute to the magnetic properties of LFIP because of its closed shell configuration.

A consideration of the ligand field splitting of the d orbitals further validates our findings (*q.v.* Figure 33b). In the ground state there are four unpaired d electrons. From the spin-only magnetic moment formula, it is predicted that LFIP would have an effective magnetic moment of approximately $\sqrt{24} = 4.9$ μ_B/Fe. Because LFIP was found to have an effective magnetic moment of 5.39 μ_B/Fe – and since most Fe^{2+} high-spin octahedra have observed effective magnetic moments between 5.1 μ_B/Fe and 5.7 μ_B/Fe[61] – our conclusions are defensible.

Optical Properties of Lithium Iron Indium Phosphate

Ultraviolet-Visible Diffuse Reflectance Spectroscopy

In order to assess the energetic properties of LFIP, a sample was subjected to reflectance spectroscopy experiments (Figure 32). UV-Vis diffuse reflectance spectroscopic measurements were taken to determine the band-gap energy of this material. Using the Indirect_E curve fitting function in IGOR PRO (coefficient values ± one standard deviation: A = 10.732 ± 0.177, Eg_indir = 2.9435 ± 0.00472) to fit the linear range of the Kubelka-Munk rescaled data (α is the absorption coefficient, s is the scattering coefficient), it was found that the band-gap energy (E_g) of LFIP is equal to 2.94 eV, or equivalently 420 nm. This band-gap energy is near the border between the visible and ultraviolet regions of the electromagnetic spectrum. This is consistent with the lack of strong coloration in the sample. Additionally, it is worth noting that E_g for LFIP is smaller than E_g for LFP (3.84 eV).[62]
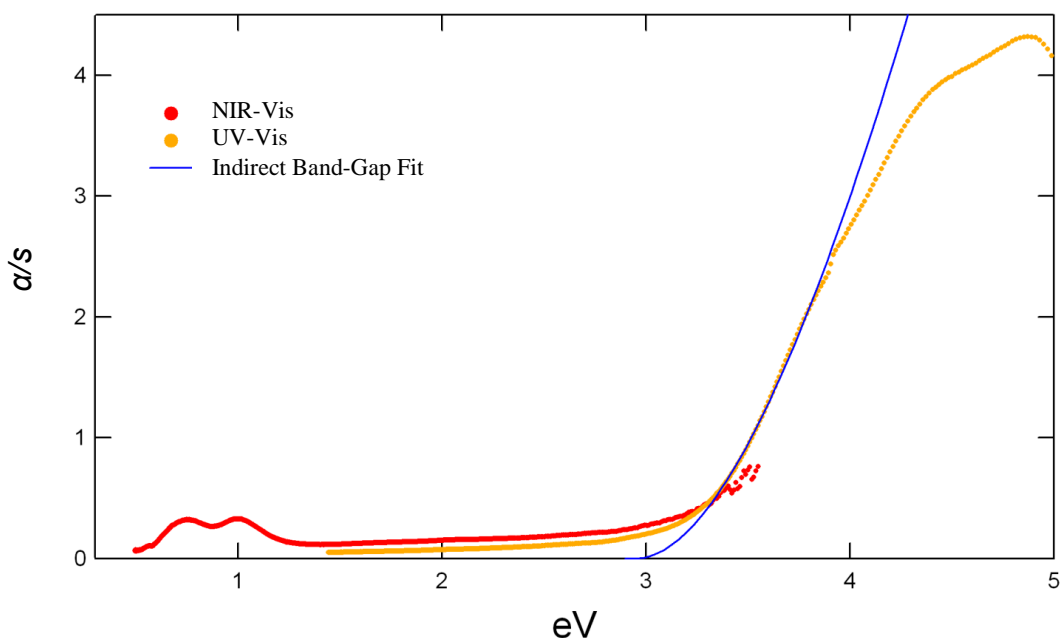
Figure 32: Determination of band-gap energy and octahedral d orbital energy level splitting of Fe^{2+} in $LiFeIn(PO_4)_2$.

Near-Infrared-Visible Reflectance Spectroscopy

NIR-Vis spectroscopic measurements were taken to study the d orbital energy level splitting in LFIP (Figure 32). Peaks were found at 0.75 eV and 0.99 eV, or equally 1650 nm and 1250 nm, respectively. Ligand field theory is essential in assigning these splitting energies. As we have noted earlier In^{3+} has a closed shell configuration, meaning that the observed splitting energies must both correspond to d electron promotions in Fe^{2+}. The ground state electron configuration of Fe^{2+} is [Ar] $3d^6$, making it a d^6 ion. We have established from structural analysis of LFIP that the cation occupies an octahedral site of O^{2-} ligands, though it must be observed that the ligand field splitting must deviate from that of an ideal octahedron, as per the observed distortion in the FeO_6 octahedra (which furthermore does not resemble a classical Jahn-Teller distortion). As is typical for iron oxides, the octahedral crystal-field splitting parameter (Δ_o) is likely smaller in magnitude than the energetic penalty arising from electron pairing (O^{2-} is a fairly weak field ligand). Consequently, it is highly probable that the Fe^{2+} cations have assumed

high-spin d electron configurations. However, the energy scheme is complicated by the fact that two splitting energies are observed, indicating that at least two significantly large transitions – and consequently three orbital levels – must be present. Such splitting is anomalous for d^6 high-spin octahedral metal complexes, since only one spin-allowed electronic transition is expected ($^5T_{2g} \rightarrow {}^5D$; *q.v.* Figure 33a). It is apparent, therefore, that the distortion in the FeO_6 octahedra is quite significant. From these considerations, an energy scheme for the ligand field splitting of the d orbitals of Fe^{2+} can be constructed (Figure 33b).
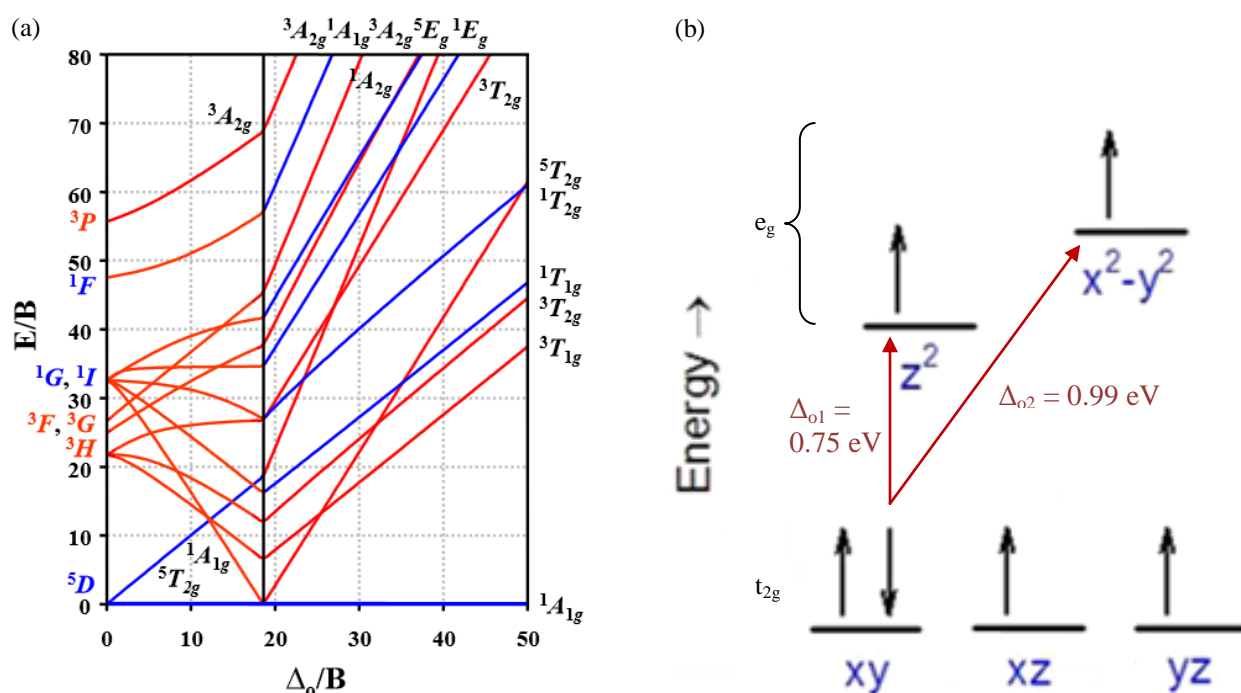
Figure 33: (a) Tanabe-Sugano diagram for a d^6 octahedral metal complex. Photo credit: <http://chemistry.bd.psu.edu/jircitano/TSdiagram.pdf>. (b) Ligand field splitting of d orbitals for octahedral Fe^{2+} in $LiFeIn(PO_4)_2$. Assignments for doubly occupied t_{2g} orbital and e_g orbitals are arbitrary.

As previously stated, at least two electronic transitions are observed from the NIR-Vis data, designated Δ_{o1} and Δ_{o2}. Since spin-allowed transitions must be ensured, the most plausible and lowest energy ligand field splitting would require the raising of energy of one of the e_g orbitals. The smaller crystal-field splitting parameter (Δ_{o1}) corresponds to the promotion of an electron from the doubly occupied t_{2g} orbital (arbitrarily selected as "xy") to the lower e_g orbital

(arbitrarily "z^2"), and the larger splitting parameter (Δ_{o2}) to the promotion of an electron to the higher e_g orbital ("x^2-y^2"). This unusually high degree of splitting can be explained by the significant distortion observed in the structurally determined FeO_6 octahedra. Moreover, the peaks at 0.75 eV and 0.99 eV are rather broad. Accordingly, it is possible that more electronic transitions may exist whose peaks are obscured at the measured resolution.

Chemical Delithiation Tests – Aqueous $K_2S_2O_8$ Treatments of Lithium Iron Indium Phosphate

As an initial assessment of the delithiation potential for LFIP, a portion of the product was treated with an over-excess of two molar equivalents of $K_2S_2O_8$ in distilled water (the Nernst standard potential of the $K_2S_2O_8$/K_2SO_4 redox couple is about 5 V *vs.* Li/Li$^+$).[63] This treatment was chosen for its relative aggressiveness and ease of implementation. The aqueous solution was stirred with a magnetic stir bar at room temperature for 65 hours. The product was then washed with distilled water and filtered with the aid of aspiration. A second portion of the same LFIP sample was likewise treated with $K_2S_2O_8$ and washed and filtered but instead subjected to continuous heating at 85-90 °C for the same period of time, so as to promote faster reaction kinetics. PXRD patterns of both treated samples were taken (Figure 34), and their refined cell parameters compared to those of untreated LFIP (Table 7). The PXRD patterns of all three samples were co-refined with LFP cell parameters to account for LFP impurities and hence improve the accuracy of the refinement of the LFIP cell parameters.

Table 7: Lattice Parameter Tracking of $LiFeIn(PO_4)_2$ through $K_2S_2O_8$ Delithiation Treatments

Sample	a (Å) (% Change)	b (Å) (% Change)	c (Å) (% Change)
$LiFeIn(PO_4)_2$	9.2832 (N/A)	13.7723 (N/A)	9.4817 (N/A)
$LiFeIn(PO_4)_2$ + $K_2S_2O_8$	9.2844 (+0.013)	13.7752 (+0.021)	9.4844 (+0.028)
$LiFeIn(PO_4)_2$ + $K_2S_2O_8$ + heat	9.2836 (+0.004)	13.7752 (+0.021)	9.4833 (+0.017)
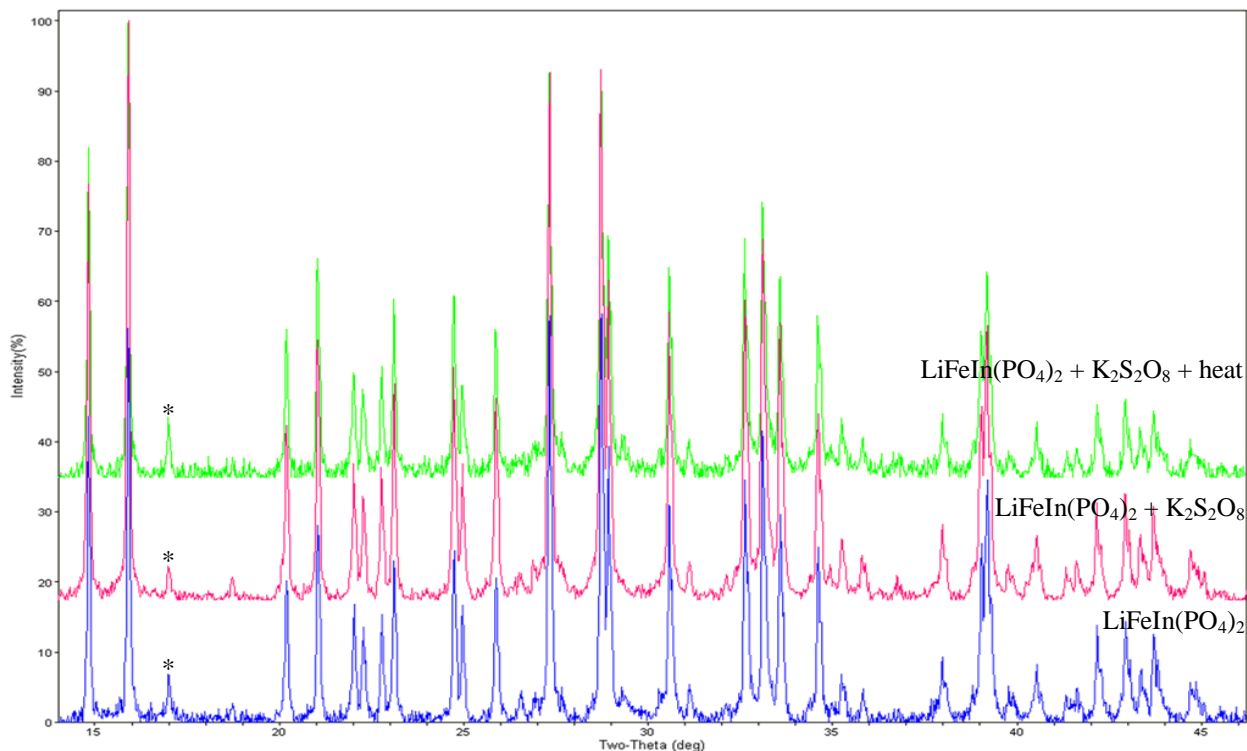
Figure 34: PXRD patterns used in assessing the effectiveness of chemical delithiation tests on $LiFeIn(PO_4)_2$. $LiFePO_4$ impurity peak is marked with an asterisk (*).

It is readily apparent that neither sample of $K_2S_2O_8$-treated LFIP – with and without heating – underwent any appreciable delithiation. The PXRD patterns show no significant change in the peak positions or relative intensities that are expected to accompany the deintercalation of Li^+ from the crystal structure. These unsuccessful "one-way" chemical delithiation attempts suggest that cyclic deintercalation-intercalation processes, including electrochemical cycling, will prove quite challenging.

Electrochemical Cycling of Lithium Iron Indium Phosphate

Given the observed resistance of LFIP to chemical delithiation measures it was determined that electrochemically-driven delithiation would need to be attempted at a fairly low cycling rate in order to increase the likelihood of Li^+ deintercalation. For the initial test it was decided to cycle the coin cells at a C-rate of C/20, between 1.5 V and 4.0 V *vs.* Li^+/Li.
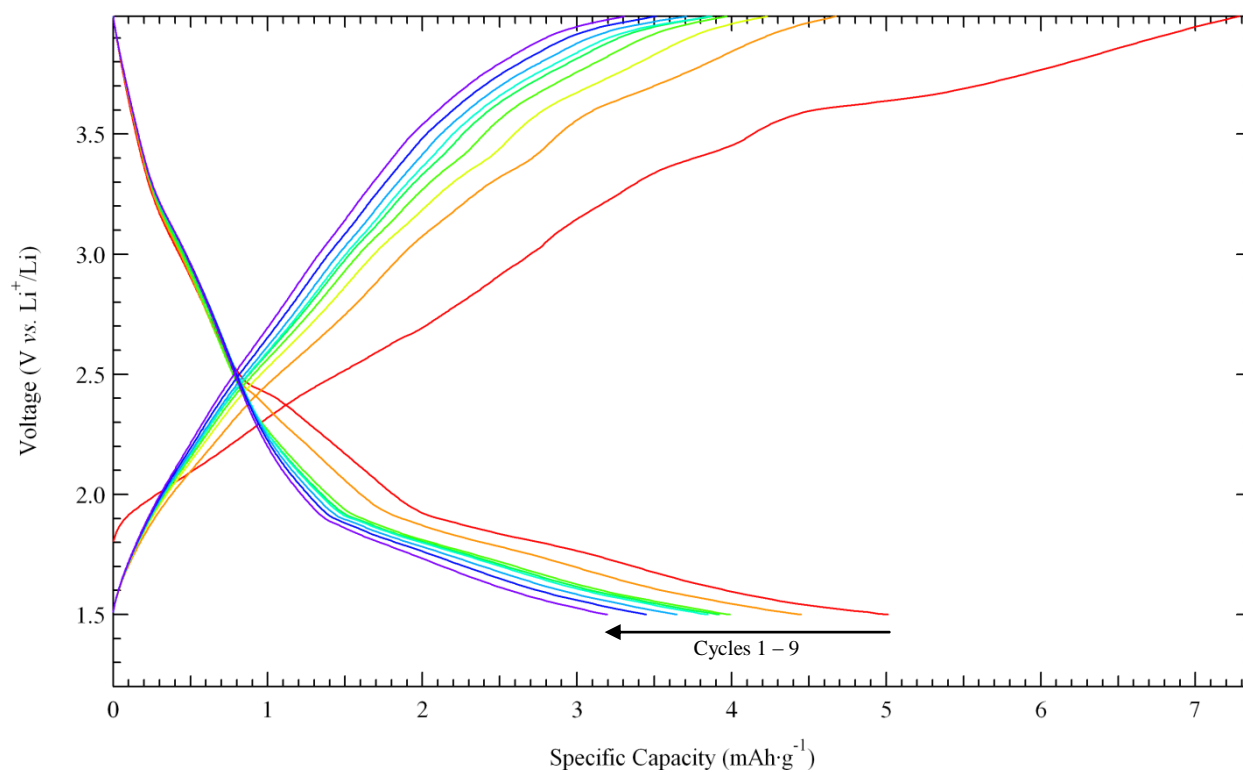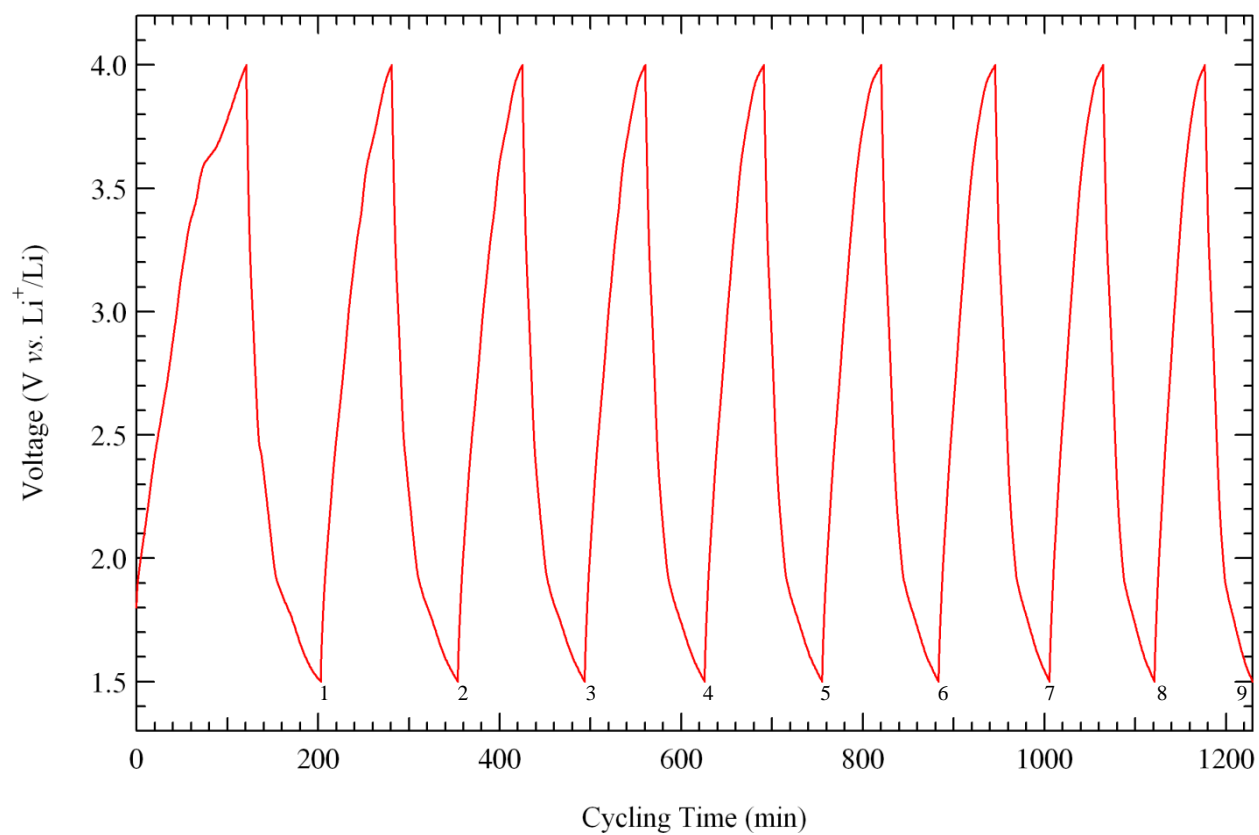
Figure 35: Electrochemical performance of LFIP when cycled between 1.5 V and 4.0 at a rate of C/20. Pictured are the cell's voltage as a function of cycling time (top) and its capacity performance (bottom).

It is evident from Figure 35 that LFIP, with a theoretical capacity of 72.9 mAh·g^{-1}, performs well below expectations. The first discharge – the best performing one – completes in 82.1 min (1.37 h), only 7% of the intended discharge time. Analogously, the specific capacity achieved upon this discharge is 5.01 mAh·g^{-1}, likewise equivalent to 7% of the theoretical capacity of LFIP. Hence, while disappointing, these results are in agreement. The specific capacity of the cathode rapidly tapers off at an average capacity loss of 5.4% per cycle, achieving only 3.19 mAh·g^{-1} (4% of theoretical capacity) after as few as nine cycles. Moreover, no plateaus were observed within the cycled voltage range, especially within the anticipated range of 2.5 V and 3.5 V. It is obvious from these measurements that LFIP is not electrochemically active.

Bond-Valence Sum Difference Map Analysis of Lithium Iron Indium Phosphate

In light of the poor performance of LFIP in both chemical delithiation and electrochemical cycling tests, BVS difference maps were calculated to examine the Li$^+$ diffusion pathways within the material. The BVS difference maps were constructed from a modified LFIP CIF file containing only the O sites using a program developed by Dr. Janssen of the Khalifah Group and relevant parameters for a Li$^+$-O^{2-} ionic bond obtained from an external website, SoftBV.[64]

(a)

(b)

(c)
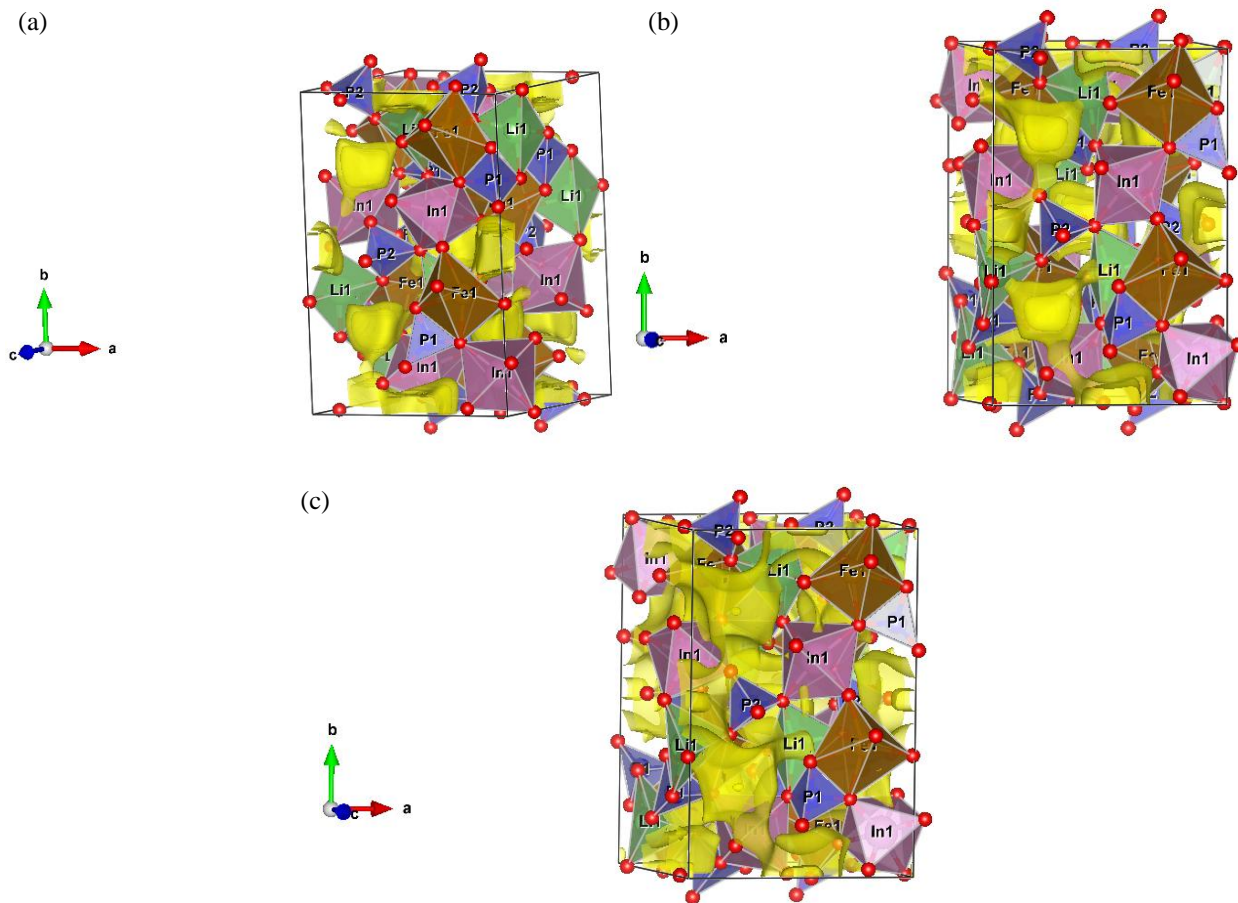
Figure 36: BVS difference maps for LiFeIn(PO$_4$)$_2$, indicating the calculated Li$^+$ diffusion pathways with thresholds of (a) 0.05 vu, (b) 0.1 vu, and (c) 0.25 vu.

Figure 36 contains the calculated BVS difference maps within the LFIP unit cell, with various isosurface levels. These maps were constructed based on the assumption of a Li$^+$ valence of 1 vu. It appears that the Li$^+$ diffusion pathways are 2D in nature and connect Li sites along the *a* and *b* directions. Table 8 lists the threshold values needed for Li$^+$ diffusion through different atomic sites. The threshold value required to form a complete diffusion channel through the unit cell is fairly low at 0.1 vu difference from ideal. However, the threshold required to avoid both Fe and In sites is quite high at 1 vu, which implies that diffusion is difficult. As a result, successful delithiation of this material would require impractically long times.

Table 8: Bond-Valence Sum Difference Map Thresholds for Li⁺ Diffusion Pathways in LiFeIn(PO₄)₂

Threshold (vu)	Diffusion Pathway
0.1	Any site
0.5	Avoid Fe sites
1	Avoid Fe and In sites

These calculations explain our experimental results. There is an apparent lack of channels for Li⁺ diffusion in LFIP, consistent with our multiple failed attempts to delithiate the sample. The predicted and observed low diffusivity of Li⁺ in LFIP is a large hindrance to the requisite combination of good ion and electron diffusion in a viable cathode. Hence, despite being a chemical relative of LFP, pristine LFIP is a poor candidate for a cathode material.

As a comparison, BVS difference maps of the Li⁺ diffusion pathways in $Li_2Ni(SO_4)_2$ indicate that a slightly higher threshold of 0.2 vu is necessary to observe clear Li⁺ channels. However, the presence of a second Li atomic site in the material allows for diffusion through only Li atomic sites at this same threshold, not at a higher value as in LFIP. This begs the question of why the material is not electrochemically active, but perhaps it is a matter of kinetics which leads the delithiation process to operate on a very long timescale.

IV. CONCLUSIONS AND FUTURE PROSPECTS

In the preceding work, $LiFeIn(PO_4)_2$ was prepared by solid-state methods and characterized. LFIP crystallizes in the primitive orthorhombic space group *Pbca* with the $Li_2Ni(SO_4)_2$ structural prototype. Its lattice parameters are $a = 9.276(1)$ Å, $b = 13.757(2)$ Å, $c = 9.476(1)$ Å, $V = 1209.13(1)$ Å^3. The atoms are arranged in distorted LiO_4 tetrahedra, distorted FeO_6 octahedra, InO_6 octahedra, and PO_4 tetrahedra, following the $Li_2Ni(SO_4)_2$ structural prototype. Each LiO_4 tetrahedron shares two of its vertices with a FeO_6 octahedron and a PO_4 tetrahedron, and shares its two remaining vertices with an InO_6 octahedron and a PO_4 tetrahedron. Each FeO_6 octahedron shares two of its edges with PO_4 tetrahedra, at each of the four vertices forming these edges a corner with an InO_6 octahedron, and at the remaining vertices a LiO_4 tetrahedron and a PO_4 tetrahedron Each InO_6 octahedron shares at four vertices a corner with a PO_4 tetrahedron and a FeO_6 octahedron and at the remaining two a corner with a LiO_4 tetrahedron and a PO_4 tetrahedron. The lack of connectivity between polyhedra of the same kind explains in several senses the observations in magnetic, optical, and delithiation experiments. LFIP is paramagnetic (5.39 μ_B/Fe) with weak antiferromagnetic properties, and does not order magnetically above 2 K. It has a band-gap energy of 2.94 eV and at least two d-d excitations at 0.75 eV and 0.99 eV. Chemical delithiation treatments with aqueous $K_2S_2O_8$ failed to produce significant structural changes in LFIP, and when electrochemically cycled between 1.5 V and 4.0 V LFIP failed to achieve any notable capacity. BVS difference mapping of the Li^+ diffusion pathways revealed that the calculated pathways are 2D, extending in both the *a* and *b* directions. However, the difference maps suggest that lower barrier Li^+ ion conductivity cannot be achieved without including Li^+ ions passing through the octahedral sites occupied and blocked by Fe^{2+} and In^{3+}.

Additional Studies of Lithium Iron Indium Phosphate and Partially-Delithiated Lithium Iron Phosphate

We have done some preliminary work in studying the structural changes associated with the partial delithiation of LFP. We have begun to track the changes in lattice parameters of the two components in an LFP-FePO$_4$ solid solution as a function of annealing time (Figure 41). GGA calculations of LFIP are underway to better understand its electronic structure. Thus far, we have obtained data for non-spin-polarized structural relaxations for it as well as for its delithiated counterpart, FeIn(PO$_4$)$_2$, but these results have limited value until data on the spin-polarized relaxations is acquired. Electron microscopy studies of pure LFIP need to be conducted to examine its morphology. Because the pristine LFIP phase does not perform well as cathode, it may be worthwhile examining whether the addition of dopants or chemical substitution will favorably alter the Li$^+$ diffusion pathways. Prior to this, the pristine material should be cycled through an overpotential to ensure that it is otherwise electrochemically inactive. Galvanostatic intermittent titration technique (GITT) studies would offer insights into battery performance, should a successful battery be developed.

Investigations into Lithium Iron Indium Phosphate-Related Compounds

Investigations need to be made into better defining the phases present in the Li$_3$PO$_4$-Fe$_3$(PO$_4$)$_2$-InPO$_4$ system and the boundaries between them. We have found evidence for four unknown phases in addition to LFIP; these compositions, when identified – and later discoveries – will need to be characterized in a likewise manner.

Structural and other characterization studies ought to be done on directly synthesized FeIn(PO$_4$)$_2$, the anticipated delithiation product of LFIP. It is evident from PXRD patterns

(Figure 42) that this phase has a different structure than LFIP. Additionally, an early attempt to synthesize "$Li_2Co_2In(PO_4)_3$," prior to the determination of the actual composition of LFIP, yielded a multiphase product with diffraction peaks similar in character to those of LFIP (Figure 42). This "LCIP" product, the Co chemical analogue to LFIP, is worth further investigation, particularly to assess similarities in structure and electrochemical behavior. Such a product is also interesting since, aside from Imaizumi and coworkers'[50] cursory discussion, the only known example of a Li-Co-In compound is a molybdate, $Li_{0.33}Co_{0.33}In_{0.34}MoO_4$, described in a review of ternary molybdates by Kozhevnikova and Mokhosoev.[65]

Furthering this line of inquiry and much in the spirit of the exploratory studies which led to the discovery of LFIP, it would be considered a worthy project to attempt to synthesize and subsequently characterize compounds belonging to the general series $LiM^{II}M^{III}(PO_4)_2$ [M^{II} = Co^{2+}, Ni^{2+}, Zn^{2+}, Cu^{2+}, Mn^{2+}, Cr^{2+}; M^{III} = Al^{3+}, Ga^{3+}, In^{3+}, V^{3+}], as well as to attempt to produce mixed sulfates/phosphates containing these cations.
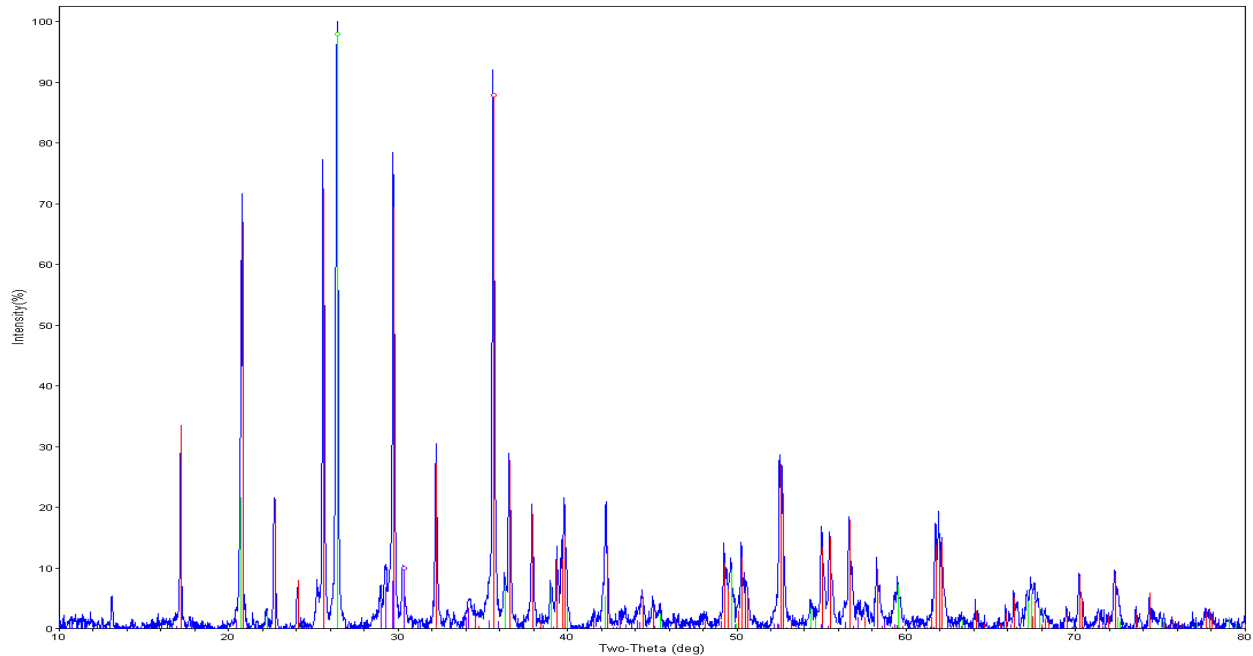
VI. SUPPLEMENTARY FIGURES AND TABLES

Figure 37: PXRD pattern for "Li$_2$Fe$_2$Al(PO$_4$)$_3$" (750 °C, 8h). Indicated are the predicted peak positions and relative intensities for LiFePO$_4$ (red, ICDD PD #01-081-1173), AlPO$_4$ (green, #01-076-0227), and Fe$_2$P$_2$O$_7$ (purple, #01-076-1762). Note that the diffraction peaks are well accounted for by these known phases.
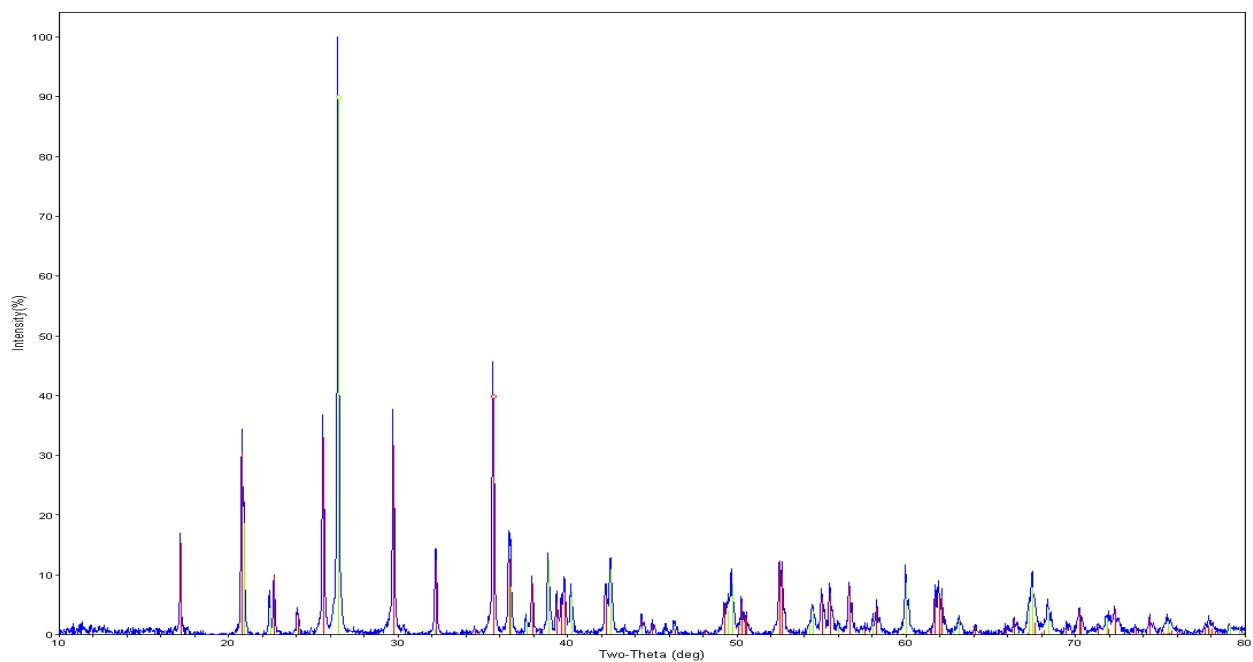
Figure 38: PXRD pattern for "Li$_2$Fe$_2$Ga(PO$_4$)$_3$" (750 °C, 8h). Indicated are the predicted peak positions and relative intensities for LiFePO$_4$ (red, ICDD PDF #01-081-1173) and GaPO$_4$ (green, #01-072-7643). Note that all diffraction peaks are well accounted for by these known phases.

50

Figure 39: PXRD pattern for "$Li_2Fe_2V(PO_4)_3$" (750 °C, 8h). Indicated are the predicted peak positions and relative intensities for $LiFePO_4$ (red, ICDD PDF #01-074-9597), $Li_3V_2(PO_4)_3$ (green, #01-072-7074), and $Fe_7(P_2O_7)_4$ (purple, #01-077-0851). Note that the diffraction peaks are well accounted for by these known phases.
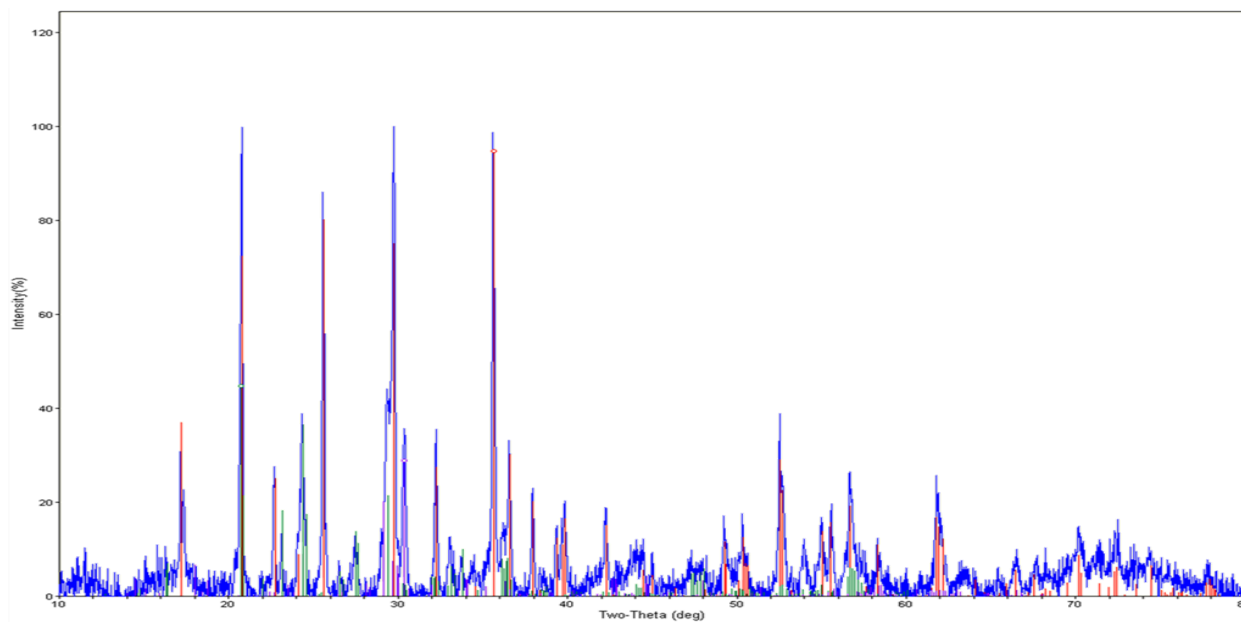

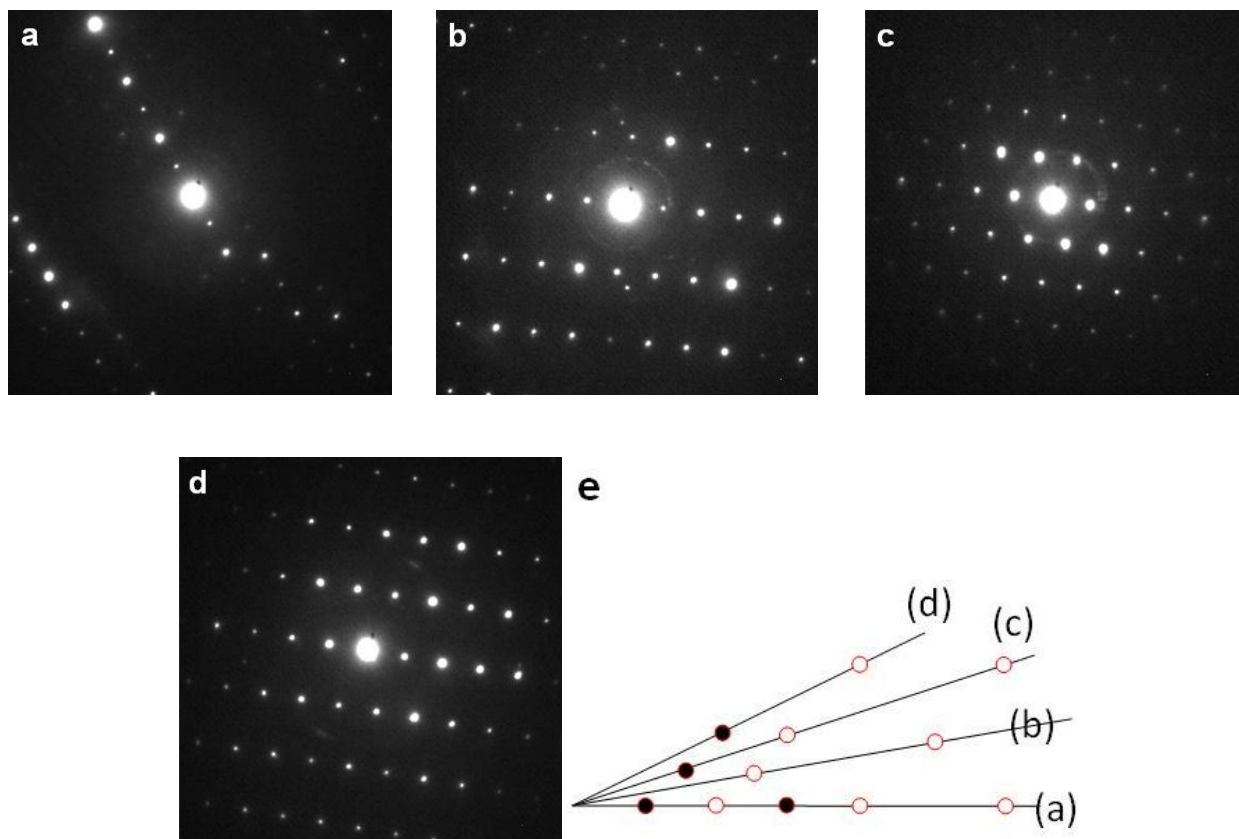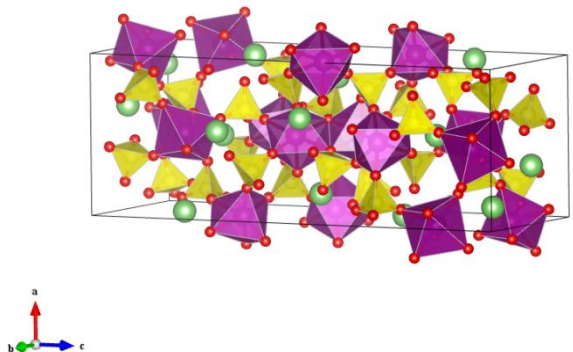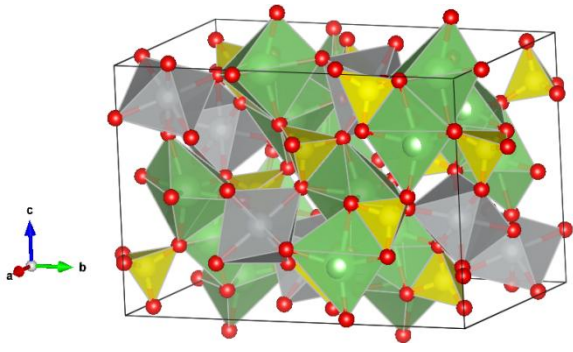**Figure 40:** (a-d) EDPs from a second, In-poorer particle found in the "$Li_{2.5}Fe_{1.75}In(PO_4)_3$" sample, with (e) corresponding reciprocal lattice plane. Suspected to be evidence for an unknown "γ" phase.

51

Table 9: Bond Angles in LFIP as Refined from Single-Crystal Data

Atom 1	Atom 2 (Vertex)	Atom 3	Bond Angle (°)	Atom 1	Atom 2 (Vertex)	Atom 3	Bond Angle (°)
O4	Fe	O5	64.27(4)	O4	P1	O5	100.66(6)
O7	Fe	O8	66.43(4)	O2	Li	O6	110.7(2)
O1	Li	O2	92.7(1)	O1	Li	O3	111.5(2)
O5	In	O8	84.23(4)	O1	Li	O6	114.0(2)
O3	In	O7	84.44(4)	O1	Fe	O6	101.98(5)
O3	Li	O6	95.1(1)	O2	P1	O4	105.89(6)
O4	Fe	O8	85.25(4)	O3	P2	O6	108.58(7)
O3	In	O8	85.79(4)	O3	P2	O7	109.30(6)
O2	In	O4	86.80(4)	O2	P1	O5	111.61(7)
O4	Fe	O7	87.35(4)	O3	P2	O8	111.86(7)
O6	Fe	O8	88.37(4)	O1	P1	O2	112.44(7)
O5	In	O7	88.55(4)	O1	P1	O4	112.03(6)
O5	Fe	O6	88.78(4)	O6	P2	O8	113.20(6)
O4	Fe	O6	89.02(4)	O1	P1	O5	113.38(6)
O4	In	O8	89.37(4)	O6	P2	O7	113.72(6)
O2	In	O7	89.67(4)	O5	Fe	O7	111.88(4)
O1	Fe	O5	90.09(4)	O1	Fe	O8	120.25(5)
O4	In	O5	91.90(4)	O2	Li	O3	133.7(2)
O1	Fe	O7	92.68(4)	O5	Fe	O8	149.43(4)
O7	In	O8	94.16(4)	O1	Fe	O4	152.07(4)
O2	In	O3	94.32(4)	O6	Fe	O7	154.75(4)
O3	In	O4	95.75(4)	O3	In	O5	167.35(4)
O2	In	O5	96.16(4)	O2	In	O8	176.16(4)
O7	P2	O8	100.00(6)	O4	In	O7	176.46(4)

Table 10: Initial Hits in Pearson's Crystal Data for LiFeIn(PO$_4$)$_2$ Structural Similarities – Good Candidates

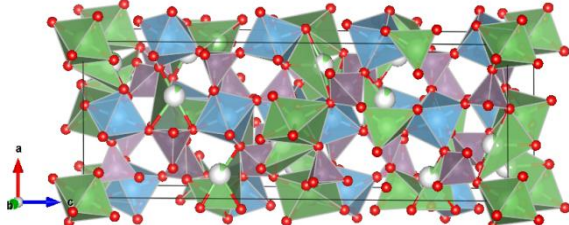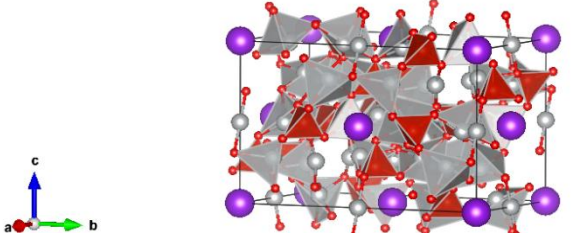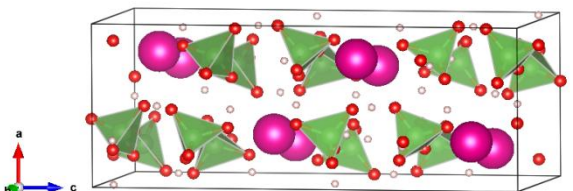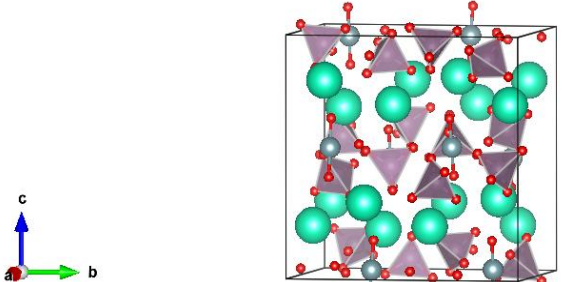| Formula	Cell Parameters	Polyhedra Connectivity	CIF Graphic	Most Recent Reference
Li$_2$Mn$_2$(SO$_4$)$_3$	a = 8.686(2) Å b = 8.792(2) Å c = 24.146(4) Å $\alpha = \beta = \gamma = 90°$ V = 1844 Å^3	Corner-sharing SO$_4$ tetrahedra to MnO$_6$ octahedra, two edge-sharing MnO$_6$ octahedra		Isasi, J.; Train, C.; Jaulmes, S.; Elfakir, A.; Quarton, M. *J. Solid State Chem.* **2001**, *158*(2), 148.
Li$_2$Ni(SO$_4$)$_2$	a = 9.126(2) Å b = 9.001(2) Å c = 13.543(3) Å $\alpha = \beta = \gamma = 90°$ V = 1112.5 Å^3	Isolated NiO$_6$ octahedra linked at corners to one (distorted) LiO$_6$ octahedron and one SO$_4$ tetrahedron. Edge-sharing LiO$_6$ octahedra form zigzag chains along *a* direction. Each LiO$_6$ octahedron shares edges with two SO$_4$ tetrahedra.		Isasi, J.; Jaulmes, S; Elfakir, A.; Quarton, M. *Z. Kristallogr. – New Cryst.Struct.* **2001**, *216*(3), 331.
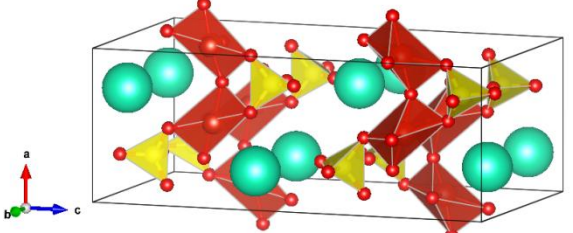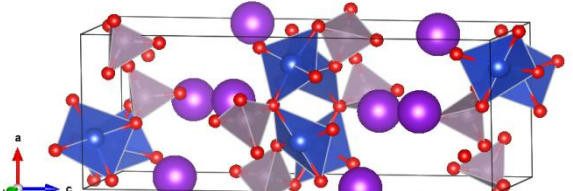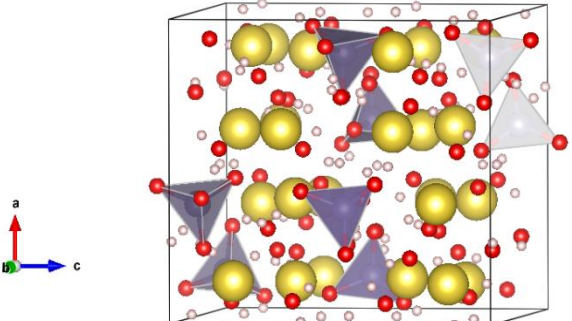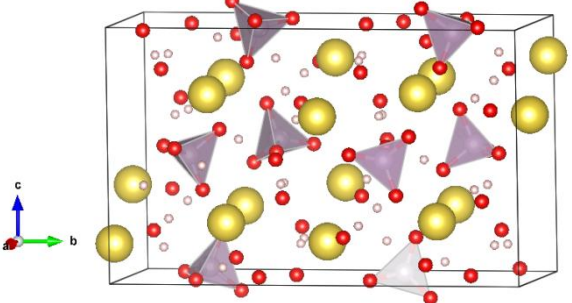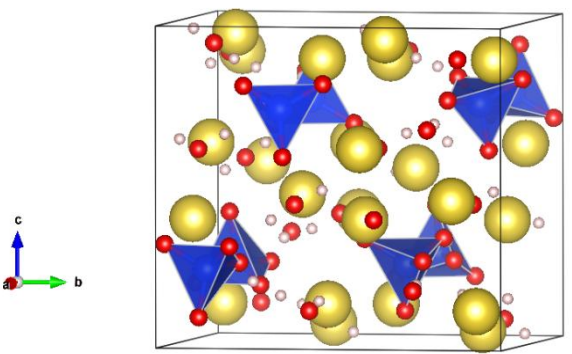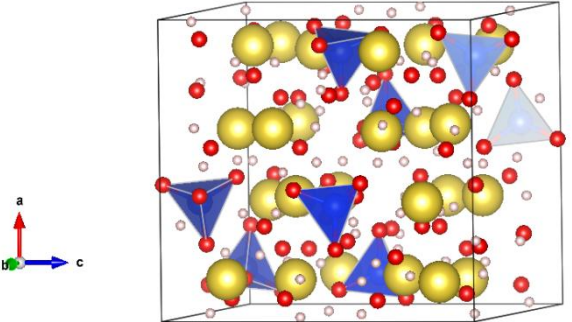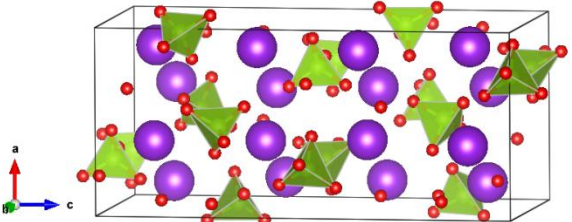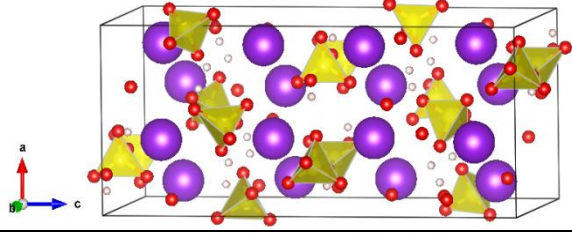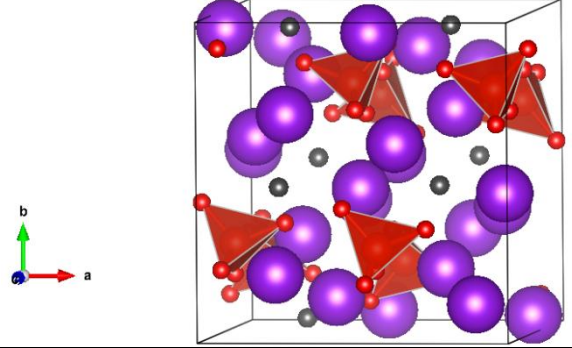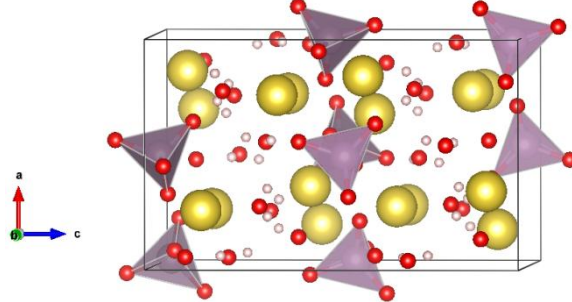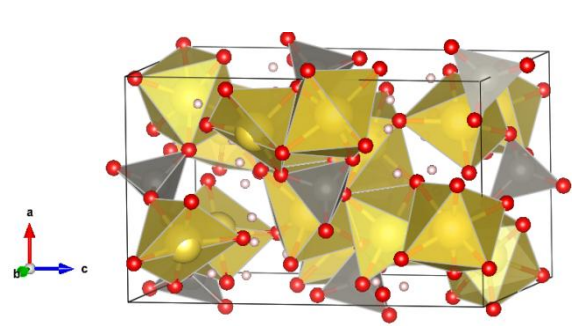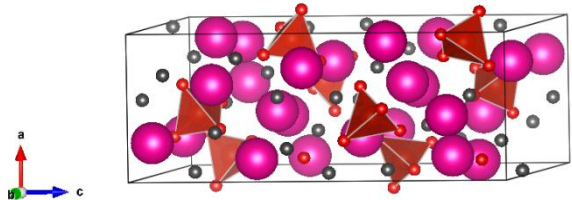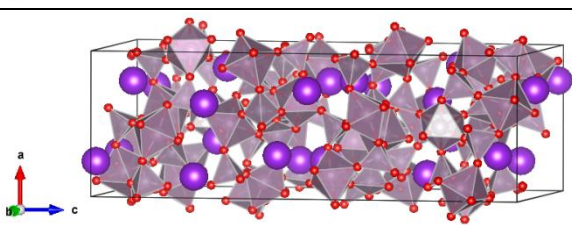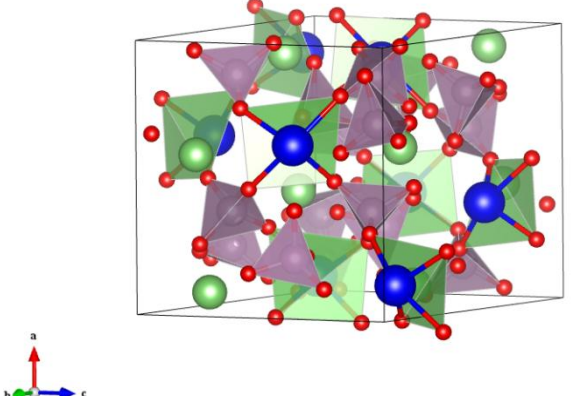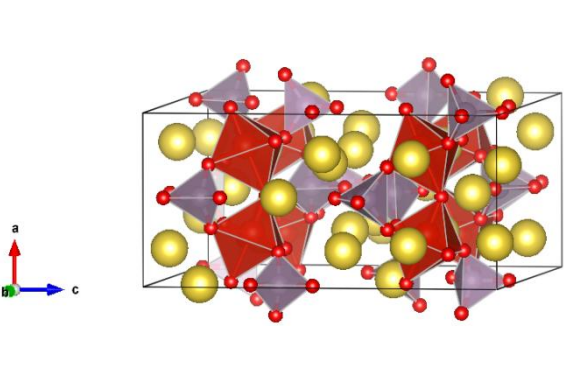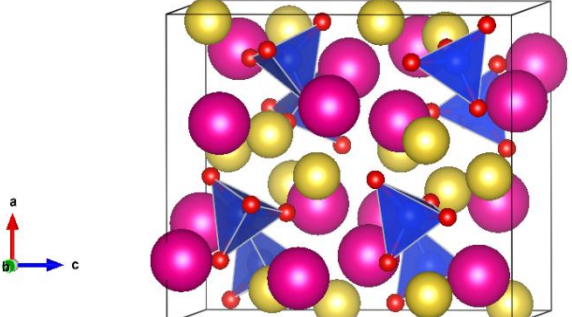
Li$_{3.56}$(PO$_4$)$_6$Ti$_4$ ~ Li$_2$Ti$_2$(PO$_4$)$_3$	$a = 8.667(3)$ Å $b = 23.968(6)$ Å $c = 8.565(2)$ Å $\alpha = \beta = \gamma = 90°$ $V = 1779.2$ Å^3	Irregular & incomplete LiO$_6$ octahedra, TiO$_6$ octahedra, PO$_4$ tetrahedra. Extensive corner-sharing, some edge-sharing between LiO$_6$ and TiO$_6$		Wang, S.; Hwu, S.-J. *Chem. Mater.* **1992**, *4*(3), 589.

Table 11: Initial Hits in Pearson's Crystal Data for LiFeIn(PO$_4$)$_2$ Structural Similarities – Disqualified Candidates

Formula	Cell Parameters	Polyhedra Connectivity	CIF Graphic	Most Recent Reference
Ag$_{11}$K(VO$_4$)$_4$	$a = 16.533(1)$ Å $b = 10.6286(7)$ Å $c = 10.5452(7)$ Å $\alpha = \beta = \gamma = 90°$ $V = 1853$ Å^3	Nothing of note		Kovalevskiy, A.; Jansen, M. *Z. Anorg. Allg. Chem.* **2006**, *632*(3), 413.
(AsO$_4$)$_2$H$_5$Rb	$a = 7.9403(8)$ Å $b = 9.8218(6)$ Å $c = 20.4244(6)$ Å $\alpha = \beta = \gamma = 90°$ $V = 1592.9$ Å^3	Nothing of note		Naili, H.; Mhiri, T. *J. Alloys Compd.* **2001**, *315*(1-2), 143.
Cs$_2$(MoO$_4$)$_2$(UO$_2$)	$a = 11.762(2)$ Å $b = 14.081(2)$ Å $c = 14.323(2)$ Å $\alpha = \beta = \gamma = 90°$ $V = 2372.2$ Å^3	Nothing of note		Krivovichev, S. V.; Burns, P. C. *Can. Mineral.* **2005**, *43*(2), 713.
CsO$_2$(SO$_4$)V	$a = 6.6688(13)$ Å $b = 10.048(2)$ Å $c = 17.680(4)$ Å $\alpha = \beta = \gamma = 90°$ $V = 1184.7$ Å^3	Irregular VO$_4$ tetrahedra; corner-sharing with VO$_4$ and SO$_4$ tetrahedra		Rasmussen, S. E.; Boghosian, S.; Nielsen, K.; Eriksen, K. M.; Fehrmann, R. *Inorg. Chem.* **2004**, *43*(12), 3697.
CuK(PO$_4$)	$a = 17.94(2)$ Å $b = 6.742(6)$ Å $c = 6.795(6)$ Å $\alpha = \beta = \gamma = 90°$ $V = 821.9$ Å^3	Nothing of note		Effenberger, H. S. *Z. Kristallogr.* **1984**, *168*(1-4), 113.

(GeO₄)H(H₂O)₅Na₃	$a = 11.889(6)$ Å $b = 11.039(2)$ Å $c = 13.090(2)$ Å $\alpha = \beta = \gamma = 90°$ $V = 1717.967$ Å³	Nothing of note		Schmid, R. L.; Wiebcke, M.; Felsche, J. *Acta Crystallogr., Sect. C.: Cryst. Struct. Commun.* **1991**, *C47*(6), 1145.
H(H₂O)₂Na₂(PO₄)	$a = 16.872(9)$ Å $b = 10.359(4)$ Å $c = 6.599(3)$ Å $\alpha = \beta = \gamma = 90°$ $V = 1153.354$ Å³	Slight irregularity in PO₄ tetrahedra; one P-O bond is longer		Catti, M.; Ferraris, G.; Franchini-Angela, M. *Acta Crystallogr., Sect. B: Struct. Crystallogr. Cryst. Chem.* **1977**, *B33*(11), 3449.
H(H₂O)₂Na₂(SiO₄)	$a = 10.380(5)$ Å $b = 10.053(3)$ Å $c = 11.414(5)$ Å $\alpha = \beta = \gamma = 90°$ $V = 1191.052$ Å³	Nothing of note		Schmid, R. L.; Szolnai, L.; Felsche, J.; Huttner, G. *Acta Crystallogr., Sect. B: Struct. Crystallogr. Cryst. Chem.* **1981**, *B37*(4), 789.
H(H₂O)₅Na₂(SiO₄)	$a = 11.780(5)$ Å $b = 10.940(4)$ Å $c = 12.958(5)$ Å $\alpha = \beta = \gamma = 90°$ $V = 1669.939$ Å³	Nothing of note		Smolin, Yu. I.; Shepelev, Yu. F.; Butikova, I. K. *Kristallografiya* **1973**, *18*(2), 281.
HK(SeO₄)	$a = 8.690(9)$ Å $b = 10.053(9)$ Å $c = 19.47(2)$ Å $\alpha = \beta = \gamma = 90°$ $V = 1700.90$ Å³	Nothing of note		Baran, J.; Lis, T. *Acta Crystallogr., Sect. C: Cryst. Struct. Commun.* **1986**, *C42*(3), 270.

Compound	Cell parameters	Notes	Structure	Reference
HK(SO₄)	$a = 8.429(3)$ Å $b = 9.807(3)$ Å $c = 18.976(6)$ Å $\alpha = \beta = \gamma = 90°$ $V = 1568.617$ Å³	Nothing of note		Payan, F.; Haser, R. *Acta Crystallogr., Sect. B: Struct. Crystallogr. Cryst. Chem.* **1976**, *B32*(6), 1875.
(H₂O)K₃(VO₄)	$a = 10.2136(8)$ Å $b = 10.4447(8)$ Å $c = 12.4878(6)$ Å $\alpha = \beta = \gamma = 90°$ $V = 1332.173$ Å³	Nothing of note		Kato, K.; Takayama-Muromachi, E. *Acta Crystallogr., Sect. C: Cryst. Struct. Commun.* **1987**, *C43*(11), 2040.
(H₂O)₂(MoO₄)Na₂	$a = 8.4780(2)$ Å $b = 10.5790(3)$ Å $c = 13.8300(4)$ Å $\alpha = \beta = \gamma = 90°$ $V = 1240.4$ Å³	Nothing of note		Capitelli, F.; Selim, M.; Makherjea, K. K. *Asian J. Chem.* **2006**, *18*(4), 2856.
(H₂O)₂Na₂(WO₄)	$a = 8.4797(5)$ Å $b = 10.5930(5)$ Å $c = 13.8527(10)$ Å $\alpha = \beta = \gamma = 90°$ $V = 1244.3$ Å³	NaO₆ octahedra and NaO₅ pyramidal polyhedra share corners with one another and WO₄ tetrahedra; some edge-sharing between NaO₆ and NaO₅		Farrugia, L. J. *Acta Crystallogr., Sect. E: Struct. Rep. Online* **2007**, *63*(6), i142.
(H₂O)₄Rb₃(VO₄)	$a = 16.255(1)$ Å $b = 17.771(1)$ Å $c = 7.002(1)$ Å $\alpha = \beta = \gamma = 90°$ $V = 2022.70$ Å³	Nothing of note		Kato, K.; Takayama-Muromachi, E. *Acta Crystallogr., Sect. C: Cryst. Struct. Commun.* **1985**, *C41*(10), 1415.
K₃Mo₄O₄(PO₄)₅	$a = 9.676(2)$ Å $b = 14.366(2)$ Å $c = 28.391(5)$ Å $\alpha = \beta = \gamma = 90°$ $V = 3946.503$ Å³	Extensive corner-sharing between isolated MoO₄ octahedra and PO₄ tetrahedra		Hoareau, T.; Leclaire, A.; Borel, M. M.; Grandin, A.; Raveau, B. *J. Solid State Chem.* **1995**, *114*(1), 61.

LaLi(MoO₄)₂	$a = 10.09$ Å $b = 9.92$ Å $c = 13.58$ Å $\alpha = \beta = \gamma = 90°$ $V = 1359.26$ Å³	Nothing of note		Klevtsova, R. F. *Kristallografiya* **1975**, *20*(4), 746.
Na₄(PO₄)₂(VO)	$a = 7.0231$ Å $b = 16.0068$ Å $c = 14.5129$ Å $\alpha = \beta = \gamma = 90°$ $V = 1631.5$ Å³	Isolated PO_4 tetrahedra share corners with VO_6 octahedra; VO_6 octahedra share corners with one another		Panin, R. V.; Shpanchenko, R. V.; Mironov, A. V.; Velikodnyi, Y. A.; Antipov, E. V.; Hadermann, J.; Tarnopolsky, V. A.; Yaroslavtsev, A. B.; Kaul, E. E.; Geibel, C. *Chem. Mater.* **2004**, *16*(6), 1048.
Na₂Rb₂(SiO₄)	$a = 9.8320(7)$ Å $b = 10.9226(6)$ Å $c = 11.1304(8)$ Å $\alpha = \beta = \gamma = 90°$ $V = 1195.3$ Å³	Nothing of note		Kerp, O.; Möller, A. *Z. Naturforsch., B: Chem. Sci.* **2006**, *61*(7), 833.

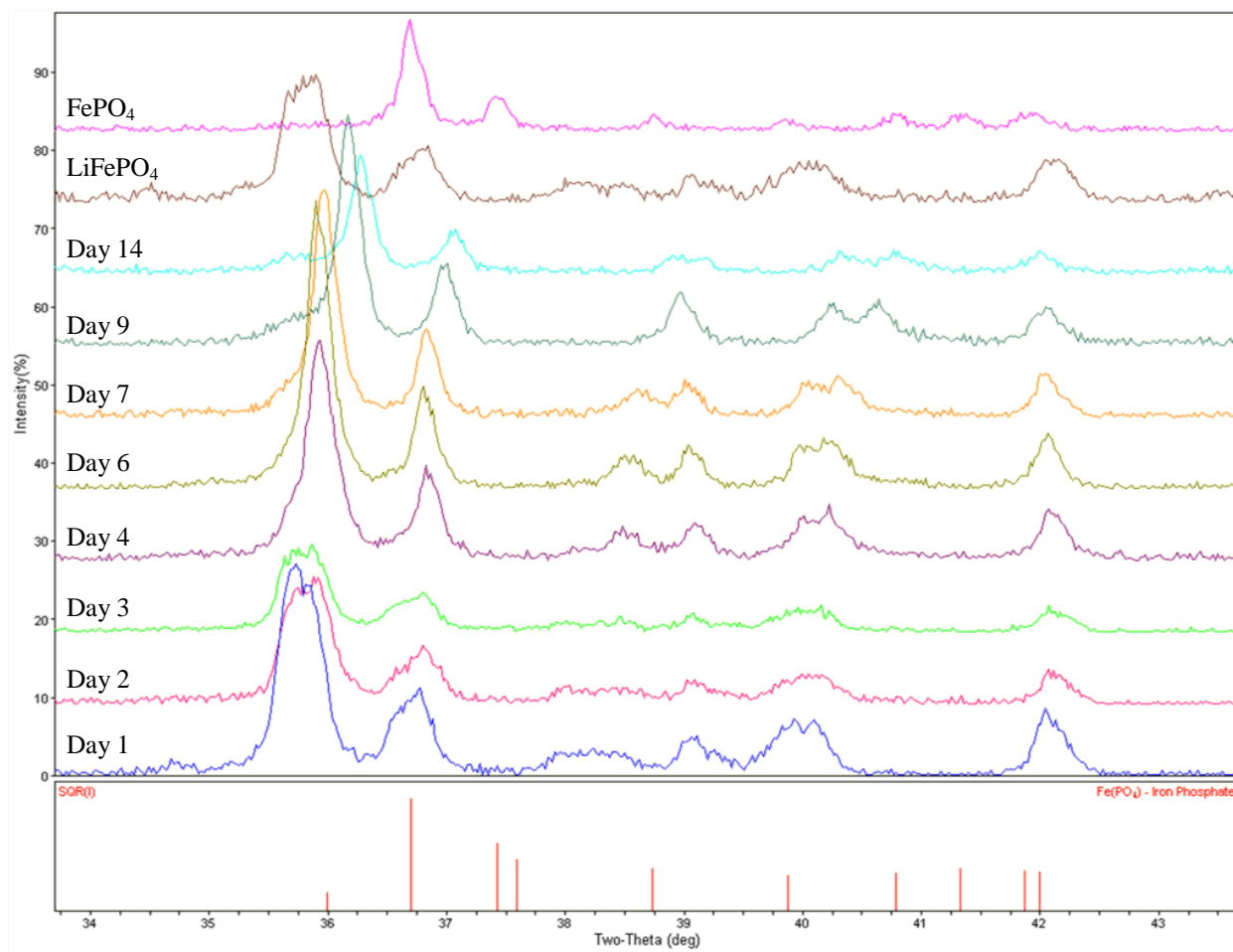**Figure 41:** Detail of PXRD patterns of $Li_{2/3}FePO_4$ over the course of annealing treatments, with $FePO_4$ example at top and typical peak positions and relative intensities at bottom (ICDD PDF #01-070-6685).
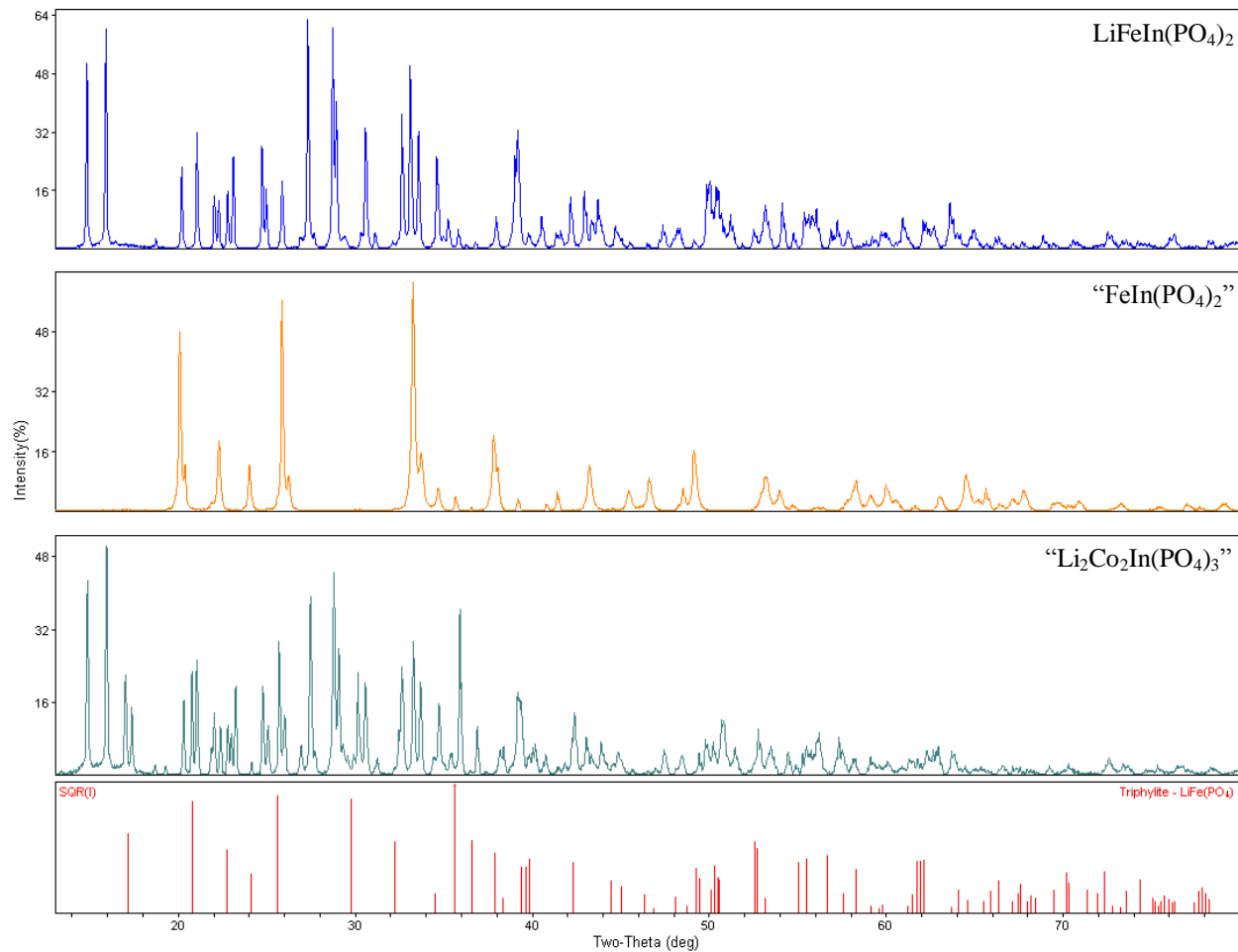
Figure 42: PXRD patterns of LiFeIn(PO$_4$)$_2$, "FeIn(PO$_4$)$_2$," and "Li$_2$Co$_2$In(PO$_4$)$_3$," with typical LiFePO$_4$ 2θ peak positions and relative intensities (ICDD PDF # 01-083-2092).

REFERENCES

[1] Nazri, Gholam-Abbas, and Gianfranco Pistoia, eds. *Lithium Batteries: Science and Technology*. Boston: Kluwer Academic, 2004. PDF.

[2] Janssen, Y.; Santhanagopalan, D.; Qian, D.; Chi, M.; Wang, X.; Hoffman, C.; Meng, Y. S.; Khalifah, P. G. *Chem. Mater.* **2013**, *25*(22), 4574.

[3] Hoang, K.; Johannes, M. *Chem. Mater.* **2011**, *23*(11), 3003.

[4] Whittingham, M. S. *Chem. Rev.* **2004**, *104*(10), 4271.

[5] Zhang, P.; Wen, Y.; Liu, J.; Xu, Q.; Ren, X.; Zhang, Q.; Luo, Z. *Xiyou Jinshu Cailiao Yu Gongcheng* **2007**, *36*(6), 954.

[6] Adams, S. *J. Solid State Electrochem.* **2010**, *14*(10), 1787.

[7] Morgan, D.; Van der Ven, A.; Ceder, G. *Electrochem. Solid-State Lett.* **2004**, *7*(2), A30.

[8] Islam, M. S.; Driscoll, D. J.; Fisher, C. A. J.; Slater, P. R. *Chem. Mater.* **2005**, *17*(20), 5085.

[9] Nishimura, S.-i.; Kobayashi, G.; Ohoyama, K.; Kanno, R.; Yashima, M.; Yamada, A. *Nat. Mater.* **2008**, *7*(9), 707.

[10] Tang, P.; Holzwarth, N. A. W.; Du, Y. A. *Phys. Rev. B: Condens. Matter* **2007**, *76*(17), 174118.

[11] Ma, Jeffrey. "Structural and Electrochemical Studies of High Voltage $Na(Ni_{2/3}Sb_{1/3})O_2$ Cathodes for Secondary Na-ion Batteries." MS thesis Stony Brook University, 2014. Print.

[12] Abruña, H. D.; Kiya, Y.; Henderson, J. C. *Physics Today* **2008**, *61*(12), 43.

[13] Padhi, A. K.; Nanjundaswamy, K. S.; Goodenough, J. B. *J. Electrochem. Soc.* **1997**, *144*(4), 1188.

[14] Padhi, A. K.; Nanjundaswamy, K. S.; Masquelier, C.; Okada, S.; Goodenough, J. B. *J. Electrochem. Soc.* **1997**, *144*(5), 1609.

[15] Amin, R.; Maier, J.; Balaya, P.; Chen, D. P.; Lin, C. T. *Solid State Ionics* **2008**, *179*(27-32), 1683.

[16] Tang, P.; Holzwarth, N. A. W. *Phys. Rev. B: Condens. Matter* **2003**, *68*(16), 165107.

[17] Perdew, J. P.; Burke, K.; Ernzerhof, M. *Phys. Rev. Lett.* **1996**, *77*(18), 3865.

[18] Anisimov, V. I.; Zaanen, J.; Andersen, O. K. *Phys. Rev. B: Condens. Matter* **1991**, *44*(3), 943.

[19] Anisimov, V. I.; Solovyev, I. V.; Korotin, M. A. *Phys. Rev. B: Condens. Matter* **1993**, *48*(23), 16929.

[20] Wang, L.; Zhou, F.; Meng, Y. S.; Ceder, G. *Phys. Rev. B: Condens. Matter* **2007**, *76*(16), 165435.

[21] Chung, S.-Y.; Choi, S.-Y.; Yamamoto, T.; Ikuhara, Y. *Phys. Rev. Lett.* **2008**, *100*(12), 125502.

[22] Liang, G.; Park, K.; Li, J.; Benson, R. E.; Vaknin, D.; Markert, J. T.; Croft, M. C. *Phys. Rev. B: Condens. Matter* **2008**, *77*(6), 64414.

[23] Li, J.; Yao, W.; Martin, S.; Vaknin, D. *Solid State Ionics* **2008**, *179*(35-36), 2016.

[24] Amin, R.; Balaya, P.; Maier, J. *Electrochem. Solid-State Lett.* **2007**, *10*(1), A13.

[25] Weichert, K.; Sigle, W.; van Aken, P. A.; Jamnik, J.; Zhu, C.; Amin, R.; Acartürk, T.; Starke, U.; Maier, J. *J. Am. Chem. Soc.* **2012**, *134*(6), 2988.

[26] Chen, G.; Song, X.; Richardson, T. J. *Electrochem. Solid-State Lett.* **2006**, *9*(6), A295.

[27] Hu, Y.; Doeff, M. M.; Kostecki, R.; Fiñones, R. *J. Electrochem. Soc.* **2004**, *151*(8), A1279.

[28] Higuchi, M.; Tsuruoka, T.; Asaka, T.; Mihara, T.; Suhara, M.; Katayama, K.; Azuma, Y. *Key Eng. Mater.* **2004**, *269*(Electroceramics in Japan VII), 147.

[29] Chen, D. P.; Maljuk, A.; Lin, C. T. *J. Cryst.Growth* **2005**, *284*(1-2), 86.

[30] Barker, J.; Saidi, M. Y.; Swoyer, J. L. *Electrochem. Solid-State Lett.* **2003**, *6*(3), A53.

[31] Biendicho, J. J.; West, A. R. *Solid State Ionics* **2011**, *203*(1), 33.

[32] Chen, J.; Graetz, J. *ACS Appl. Mater. Interfaces* **2011**, *3*(5), 1380.

[33] Morgan, D.; Van der Ven, A.; Ceder, G. *Electrochem. Solid-State Lett.* **2004**, *7*(2), A30.

[34] Jensen, K. M. Ø.; Christensen, M.; Gunnlaugsson, H. P.; Lock, N.; Bøjesen, E. D.; Proffen, T.; Iversen, B. B. *Chem. Mater.* **2013**, *25*(11), 2282.

[35] Gardiner, G. R.; Islam, M. S. *Chem. Mater.* **2010**, *22*(3), 1242.

[36] Harrison, K. L.; Bridges, C. A.; Paranthaman, M. P.; Segre, C. U.; Katsoudas, J.; Maroni, V. A.; Idrobo, J. C.; Goodenough, J. B.; Manthiram, A. *Chem. Mater.* **2013**, *25*(5), 768.

[37] Jin, C.; Zhang, X.-d.; He, W.; Wang, Z.; Hou, Y.-k. *Shandong Taoci* **2013**, *36*(4), 15.

[38] Chen, J.; Vacchio, M. J.; Wang, S.; Chernova, N.; Zavalij, P. Y.; Whittingham, M. S. *Solid State Ionics* **2008**, *178*(31-32), 1676.

[39] Wang, W.; Fan, W. CN 103647076 (A), 2014.

[40] Winand, J. M.; Rulmont, A.; Tarte, P. *J. Solid State Chem.* **1990**, *87*(1), 83.

[41] Naganovskii, Yu. K.; Sigarev, S. E. *Solid State Ionics* **1992**, *50*(1-2), 1.

[42] Sigaryov, S. E. *Mater. Sci. Eng., B* **1992**, *B13*(2), 121.

[43] Pronin, I. S.; Vashman, A. A.; Sigaryov, S. E. *Phys. Rev. B: Condens. Matter* **1993**, *48*(22), 16463.

[44] Kravchenko, V. V.; Sigaryov, S. E. *J. Mater. Sci.* **1994**, *29*(22), 6004.

[45] Potapova, A.; Novoselov, A.; Zimina, G. *J. Am. Ceram. Soc.* **2011**, *94*(5), 1317.

[46] Potapova, A. M.; Zimina, G. V.; Smirnova, I. N.; Spiridonov, F. M.; Fedorov, P. P. *Russ. J. Inorg. Chem.* **2011**, *56*(9), 1453.

[47] Paolella, A.; Bertoni, G.; Dilena, E.; Marras, S.; Ansaldo, A.; Manna, L.; George, C. *Nano Lett.* **2014**, *14*(3), 1477.

[48] Kang, C.-S.; Kim, C.; Kim, J.-E.; Lim, J.-H.; Son, J.-T. *J. Phys. Chem. Solids* **2013**, *74*(4), 536.

[49] Slobodyanik, N. S.; Nagornyi, P. G.; Korniyenko, Z. I.; Boiko, R. S.; Ivanenko, O. P.; Zatovskii, I. V.; Ogorodnik, I. V. *Ukr. Khim. Zh.* **2006**, *72*(5-6), 11.

[50] Imaizumi, S.; Toya, H.; Kuzuo, R. JP 2010067374 (A), 2010.

[51] Bosacka, M. *Thermochim. Acta* **2011**, *523*(1-2), 137.

[52] Triangular phase diagram template source: http://www.phasediagram.dk/triangular.xlsx

[53] Eyob, P.; Andersson, A. S.; Thomas, J. O. *J. Mater. Chem.* **2002**, *12*(8), 2343.

[54] P. Villars, K. Cenzual, Pearson's Crystal Data – Crystal Structure Database for Inorganic Compounds, Release 2010/11, ASM International, Materials Park, Ohio, USA.

[55] Isasi, J.; Jaulmes, S.; Elfakir, A.; Quarton, M. *Z. Krist.- New Cryst. Struct.* **2001**, *216*(3), 331.

[56] Reynaud, M.; Ati, M.; Melot, B. C.; Sougrati, M. T.; Rousse, G.; Chotard, J.-N.; Tarascon, J.-M. *Electrochem. Commun.* **2012**, *21*, 77.

[57] Reynaud, M.; Rousse, G.; Chotard, J.-N.; Rodriguez-Carvajal, J.; Tarascon, J.-M. *Inorg. Chem.* **2013**, *52*(18), 10456.

[58] Reynaud, M.; Rodriguez-Carvajal, J.; Chotard, J.-N.; Tarascon, J.-M.; Rousse, G. *Phys. Rev. B: Condens. Matter* **2014**, *89*(10), 104419.

[59] Lander, L.; Reynaud, M.; Rousse, G.; Sougrati, M. T.; Laberty-Robert, C.; Messinger, R. J.; Deschamps, M.; Tarascon, J.-M. *Chem. Mater.* **2014**, *26*(14), 4178.

[60] Reynaud, M.; Rodriguez-Carvajal, J.; Chotard, J.-N.; Tarascon, J.-M.; Rousse, G. *Phys. Rev. B: Condens. Matter* **2014**, *89*(10), 104419.

[61] "Magnetic Moments." *Coordination Chemistry Course Online.* Department of Chemistry, University of the West Indies, 10 Feb. 2014. Web. 12 Aug. 2014.

[62] Zaghib, K.; Mauger, A.; Goodenough, J. B.; Gendron, F.; Julien, C. M. *Chem. Mater.* **2007**, *19*(15), 3740.

[63] Dodd, J. L.; Yazami, R.; Fultz, B. *Electrochem. Solid-State Lett.* **2006**, *9*(3), A151.

[64] "Softness Sensitive Bond Valence Parameters." *SoftBV 0.96*. N.p., Feb. 2004. Web. 7 Aug. 2014.

[65] Kozhevnikova, N. M.; Mokhosoev, M. V. *Zh. Neorg. Khim.* **1992**, *37*(11), 2395.